

Quarterly Technical Report

Solid State Research

1999:3

Lincoln Laboratory

MASSACHUSETTS INSTITUTE OF TECHNOLOGY

LEXINGTON, MASSACHUSETTS



Prepared for the Department of the Air Force under Contract F19628-95-C-0002.

Approved for public release; distribution is unlimited.

19991228 065

DTIC QUALITY INSPECTED 2

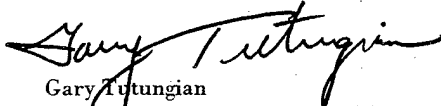
This report is based on studies performed at Lincoln Laboratory, a center for research operated by Massachusetts Institute of Technology. The work was sponsored by the Department of the Air Force under Contract F19628-95-C-0002.

This report may be reproduced to satisfy needs of U.S. Government agencies.

The ESC Public Affairs Office has reviewed this report, and it is releasable to the National Technical Information Service, where it will be available to the general public, including foreign nationals.

This technical report has been reviewed and is approved for publication.

FOR THE COMMANDER


Gary Tutungian
Administrative Contracting Officer
Plans and Programs Directorate
Contracted Support Management

Non-Lincoln Recipients

PLEASE DO NOT RETURN

Permission is given to destroy this document
when it is no longer needed.

MASSACHUSETTS INSTITUTE OF TECHNOLOGY
LINCOLN LABORATORY

SOLID STATE RESEARCH

QUARTERLY TECHNICAL REPORT

1 MAY — 31 JULY 1999

ISSUED 17 DECEMBER 1999

Approved for public release; distribution is unlimited.

LEXINGTON

MASSACHUSETTS

ABSTRACT

This report covers in detail the research work of the Solid State Division at Lincoln Laboratory for the period 1 May through 31 July 1999. The topics covered are Quantum Electronics, Electro-optical Materials and Devices, Submicrometer Technology, Biosensor and Molecular Technologies, Advanced Imaging Technology, Analog Device Technology, and Advanced Silicon Technology. Funding is provided by several DoD organizations—including the Air Force, Army, BMDO, DARPA, Navy, NSA, and OSD—and also by the DOE, NASA, and NIST.

TABLE OF CONTENTS

Abstract	iii
List of Illustrations	vii
List of Tables	x
Introduction	xi
Reports on Solid State Research	xiii
Organization	xxv
 1. QUANTUM ELECTRONICS	 1
1.1 Passively <i>Q</i> -Switched 214.8-nm Nd:YAG/Cr ⁴⁺ :YAG Microchip-Laser System for the Detection of NO	 1
 2. ELECTRO-OPTICAL MATERIALS AND DEVICES	 9
2.1 Effects of Crosstalk in Demultiplexers for Photonic A/D Converters	9
 3. SUBMICROMETER TECHNOLOGY	 17
3.1 Advanced Reticle for 157-nm Lithography	17
3.2 Vacuum-Ultraviolet Absorbance of Photoresist Compounds	20
 4. BIOSENSOR AND MOLECULAR TECHNOLOGIES	 27
4.1 Nanopores for DNA Sequencing	27
 5. ADVANCED IMAGING TECHNOLOGY	 33
5.1 Bridge Bonding of Geiger-Mode Avalanche Photodiode Arrays to CMOS Timing Circuits	 33
 6. ANALOG DEVICE TECHNOLOGY	 39
6.1 Digital Logic Operating at Data Rates up to 160 GHz	39

TABLE OF CONTENTS (Continued)

7.	ADVANCED SILICON TECHNOLOGY	43
7.1	New Low-Power 0.35- μm CCD/FDSOI-CMOS Technology	43

LIST OF ILLUSTRATIONS

Figure No.		Page
1-1	Schematic of 1.074- μm passively Q -switched microchip laser.	2
1-2	Theoretical reflectivity of output coupler.	4
1-3	Spectral runoff of optical coater with and without 6.5-cm distribution shield.	5
1-4	Spectral properties of output coatings on 12 microchip lasers (circles) and radially collocated witness samples (lines).	6
1-5	Photograph of optical head of 214.8-nm fifth-harmonic microchip laser source.	7
2-1	Photonic analog-to-digital converter systems with optical demultiplexers to increase sampling rate: (a) time-division demultiplexed and (b) wavelength-division demultiplexed systems.	10
2-2	Sampling function for capturing an input signal. Sampling rate is f_s and demultiplexing ratio is N . An amplitude weighting error ϵ is shown.	12
2-3	Decomposition of time-domain sampling function into (a) a perfect function $W(t)$ and (b) an error function $E(t)$.	12
2-4	Weighting function for one of the parallel channels of a demultiplexed photonic A/D converter system in which there is crosstalk at a level c and a time delay τ . The error is decomposed into an in-phase error ϵ_r and an out-of-phase error ϵ_i .	14
3-1	Transmission of modified fused silica and uv-grade fused silica in the vacuum-ultraviolet range. The theoretical Urbach tail fit is also shown (see text for details).	18
3-2	Absorbance spectrum for (base e) poly(ethylene) (based on numerical data in Ref. 8).	22
4-1	(a) Schematic diagram of DNA strand being drawn through ion channel. (b) Measured current trace from DNA strand moving through lipid bilayer membrane. (c) Conceptual schematic diagram of current trace indicating identification of individual bases in DNA strand.	28

LIST OF ILLUSTRATIONS (Continued)

Figure No.		Page
4-2	Fabrication process using a silicon-on-insulator substrate and relying on tight control of the top silicon layer thickness for eventual control of pit dimensions.	30
4-3	Fabrication process using a conventional silicon substrate but requiring a chemical-mechanical polishing step to planarize the membrane.	31
4-4	(a) Silicon tip formed by wet anisotropic etch; base diameter is 2 μm . (b) Silicon tip formed by isotropic plasma etch; base diameter is 2 μm . (c) Underside of wet-etched tip-shaped depression in silicon nitride membrane, with close-up of tip region. (d) Plan view TEM of completed nanopore with diameter of 20 nm.	32
5-1	Steps in the bridge-bonding process.	34
5-2	Silicon wafer which has had chips bonded to it and then undergone thinning.	36
5-3	Sloped epoxy etch.	36
5-4	Bridge-bonded pixels viewed from the avalanche photodiode side.	37
6-1	Schematic cross section of the existing Lincoln Laboratory superconducting electronics process showing the Nb(M2)/AlO _x /Nb(M3) trilayer, the Pt/Ti (R1) resistors, the Nb wiring (M4) layer, and the self-aligned contact to the counter-electrode (M3) layer.	41
6-2	Optical micrograph showing a superconducting chip as fabricated at Lincoln Laboratory. The chip fits in a 24-pin probe that is immersed in liquid helium for testing at 4.2 K. The expanded region is a photomicrograph showing the detailed layout of the tested circuit.	41
6-3	Along the left axis, the input voltage V_{in} and twice the output voltage V_{out} were plotted against the input current to show that the frequency of the output bit stream was exactly half the frequency of the input bit stream. Along the right axis, the difference between twice V_{out} and V_{in} is plotted on a 10 \times magnified scale to show the clear departure from zero, corresponding to failure of proper circuit operation, above 330 μV or 160 GHz.	42

LIST OF ILLUSTRATIONS (Continued)

Figure No.		Page
7-1	Schematic cross section of merged charge-coupled device (CCD) and 0.35- μm FDSOI-CMOS <i>n</i> - and <i>p</i> -channel transistors.	43
7-2	Image of Lexington Minuteman statue taken by 512×1024 , 15×15 - μm pixel CCD array fabricated in the new CCD/FDSOI-CMOS technology. CCD parallel and serial register clocking was done with 3.3 V.	44
7-3	CCD dark current as a function of temperature for the new CCD/FDSOI-CMOS imagers (circles) and for the standard Lincoln Laboratory CCD-only process (line).	45
7-4	(a) Typical subthreshold characteristics for SOI CMOS devices from the CCD/FDSOI-CMOS process; $W/L = 8 \mu\text{m}/0.35 \mu\text{m}$. (b) Typical output characteristics for SOI CMOS devices from the CCD/FDSOI-CMOS process; $W/L = 8 \mu\text{m}/0.35 \mu\text{m}$.	46
7-5	Ring oscillator (fanout = 1) stage delay as a function of power supply voltage for 0.35- μm CCD/FDSOI-CMOS (triangles) and commercial bulk CMOS (circle). For 3.3-V operation, the CCD/FDSOI-CMOS process is 2 times faster than the bulk process. For the same stage delay, the CCD/FDSOI-CMOS oscillator consumes 4.8 times less power than the commercial bulk process.	47

LIST OF TABLES

Table No.		Page
3-1	Optical Materials Targets for 157-nm Lithography	17
3-2	Summary of 157-nm Durability Tests for Modified Fused Silica Material for Reticle Applications	19
3-3	Summary of Photon Absorption Characteristics of Several Ground State Electrons as Determined by X-Ray Photoelectron Spectroscopy	21
3-4	Summary of Absorption Coefficients and Photon Penetration Depths Measured for a Variety of Commercially Available Resists	23
3-5	Absorption Coefficients A at 157 nm for a Number of Different Polymers	24
3-6	Absorption Cross Sections Measured at Both 157 and 193 nm for a Number of Different Photoacid Generator Molecules	25

INTRODUCTION

1. QUANTUM ELECTRONICS

A passively Q -switched 214.8-nm Nd:YAG/Cr⁴⁺:YAG microchip-laser system that uses the fifth harmonic of the 1.074- μ m transition in Nd:YAG to detect NO at the few-parts-per-billion level has been designed, constructed, and tested. A significant challenge was the development of an environmentally stable coating to provide the necessary discrimination between the 1.074- μ m laser line and the stronger transition at 1.064 μ m.

2. ELECTRO-OPTICAL MATERIALS AND DEVICES

Development is under way for a new generation of high-sampling-rate analog-to-digital (A/D) converters that exploit the unique features provided by optical sampling of electrical signals. Both time-division and wavelength-division demultiplexers must yield low crosstalk between the parallel output channels in order to yield accurate A/D conversion; an analysis predicts the level and form of the resulting errors.

3. SUBMICROMETER TECHNOLOGY

A new fluorine-containing fused silica material has been shown to satisfy initial transmission and durability requirements for use as a reticle in a 157-nm lithography system. The use of SiO₂ for a reticle material is preferred over single-crystal fluorides whose high thermal expansion coefficients lead to unacceptable pattern distortion during e-beam writing and wafer exposure.

The vacuum-ultraviolet absorption coefficients have been measured for a number of materials that might be used to formulate new photoresists for 157-nm lithography. An empirical approach has been developed for estimating the absorbances of multicomponent formulations as well as materials not yet synthesized.

4. BIOSENSOR AND MOLECULAR TECHNOLOGIES

Semiconductor-based nanometer-sized pores are being developed for use in high-speed sequencing of single DNA molecules. Structures have been fabricated that, when used with a reactive ion etch technique developed at Harvard University, will contain pores with a diameter on the order of 30 Å, the diameter of a DNA strand.

5. ADVANCED IMAGING TECHNOLOGY

A process for integrating thinned back-illuminated arrays of Geiger-mode avalanche photodiodes (APDs) to read-out integrated circuit arrays (ROIC) has been demonstrated. The process involves face-to-face epoxying of the APD array to the ROIC, removing the APD wafer substrate, etching vias between the

APDs, and patterning metallization over the sides of these vias to connect each APD to the corresponding ROIC cell.

6. ANALOG DEVICE TECHNOLOGY

Superconducting circuits operating at clock speeds up to 160 GHz have been fabricated using all-optical lithographic methods. The fabrication technology that we used is conducive to large integration scales.

7. ADVANCED SILICON TECHNOLOGY

Charge-coupled device (CCD) imager and fully depleted silicon-on-insulator (FDSOI) CMOS fabrication on the same 150-mm-diam wafer has been demonstrated for the first time. This low-power, merged process was achieved by fabricating 512×1024 -pixel CCD imagers with charge-transfer efficiency of over 99.998% and $0.35\text{-}\mu\text{m}$ CMOS ring oscillators with stage delays of 47 ps at 3.3 V and 68 ps at 2 V.

REPORTS ON SOLID STATE RESEARCH

1 MAY THROUGH 31 JULY 1999

PUBLICATIONS

InAs-Doped Silica Films for
Saturable Absorber Applications

I. P. Bilinsky
J. G. Fujimoto
J. N. Walpole
L. J. Missaggia

Appl. Phys. Lett. **74**, 2411
(1999)

Growth and Morphology of Er-Doped
GaN on Sapphire and Hydride Vapor
Phase Epitaxy Substrates

R. Birkhahn*
R. Hudgins*
D. Lee*
A. J. Steckl*
R. J. Molnar
A. Saleh*
J. M. Zavada*

J. Vac. Sci. Technol. B
17, 1195 (1999)

Optical Materials and Coatings at
157 nm

T. M. Bloomstein
V. Liberman
M. Rothschild
D. E. Hardy
R. B. Goodman

Proc. SPIE **3676**, 342
(1999)

Optical Detection of Electron
Paramagnetic Resonance in
Electron-Irradiated GaN

C. Bozdog*
H. Przybylinska*
G. D. Watkins*
V. Härle*
F. Scholz*
M. Mayer*
M. Kamp*
R. J. Molnar
A. E. Wickenden*
D. D. Koleske*
R. L. Henry*

Phys. Rev. B **59**, 12479
(1999)

*Author not at Lincoln Laboratory.

Thermomechanical Distortions of
Advanced Optical Reticles During
Exposure

J. Chang*
A. Abdo*
B. Kim*
T. Bloomstein
R. Engelstad*
E. Lovell*
W. Beckman*
J. Mitchell*

Proc. SPIE **3676**, 756
(1999)

Effects of Implant Spacer on
InP-Based Self-Aligned
Pseudomorphic SIGFETs

C. L. Chen
L. J. Mahoney
S. D. Calawa
K. M. Molvar

Electron. Lett. **35**, 746 (1999)

Spectral Beam Combining of
Yb-Doped Fiber Lasers in an External
Cavity

C. C. Cook
T. Y. Fan

*Trends in Optics and
Photonics Series*,
M. M. Fejer, H. Injeyan, and
U. Keller, eds. (Optical
Society of America,
Washington, D.C., 1999)

Origin of Exchange Field Reductions
in Diluted Magnetic Garnets

G. F. Dionne

J. Appl. Phys. **85**, 4627
(1999)

Magnetic Design for Low-Field
Tunability of Microwave Ferrite
Resonators

G. F. Dionne
D. E. Oates

J. Appl. Phys. **85**, 4856
(1999)

Screening of DNQ/Novolac Resists
with E-Beam Exposure

T. H. Fedynyshyn
S. P. Doran
M. L. Lind
T. M. Lyszczarz
W. F. DiNatale
D. Lennon
C. Sauer*
J. Meute*

Proc. SPIE **3678**, 1273
(1999)

*Author not at Lincoln Laboratory.

A FT-IR Method to Determine Dill's
C Parameter for DNQ/Novolac
Resists with E-Beam
and I-Line Exposure

T. H. Fedynyshyn
S. P. Doran
C. A. Mack*

Proc. SPIE **3678**, 1263
(1999)

Pattern Asymmetries in Phase-Edge
Imaging

M. Fritze
S. Cann
P. Wyatt

Proc. SPIE **3679**, 567
(1999)

Plasma Enhanced Chemically Vapor
Deposited Thin Films for
Microelectromechanical Systems
Applications with Tailored Optical,
Thermal, and Mechanical Properties

M. W. Horn
R. B. Goodman
M. Rothschild

J. Vac. Sci. Technol. B
17, 1045 (1999)

A Study of Resist Outgassing as a
Function of Differing Photoadditives

F. M. Houlihan*
I. L. Rushkin*
R. S. Hutton*
A. G. Timko*
O. Nalamasu*
E. Reichmanis*
A. H. Gabor*
A. N. Medina
S. Malik*
M. Neiser*
R. R. Kunz
D. K. Downs

J. Photopolym. Sci. Technol.
12, 525 (1999); *Proc. SPIE*
3678, 264 (1999)

Surface Functionalization and
Imaging Using Monolayers and
Surface-Grafted Polymer Layers

M. D. K. Ingall*
C. H. Honeyman*
J. V. Mercure*
P. A. Bianconi*
R. R. Kunz

J. Am. Chem. Soc. **121**, 1607
(1999)

*Author not at Lincoln Laboratory.

Effect of Growth Temperature on Point Defect Density of Unintentionally Doped GaN Grown by Metalorganic Chemical Vapor Deposition and Hydride Vapor Phase Epitaxy	V. A. Joshkin* C. A. Parker* S. M. Bedair* J. F. Muth* I. K. Shmagin* R. M. Kolbas* E. L. Piner* R. J. Molnar	<i>J. Appl. Phys.</i> 86 , 281 (1999)
Dry Etching of Photoresists	R. R. Kunz	In <i>Microlithography: Science and Technology</i> , J. R. Sheats and B. W. Smith, eds. (Marcel Dekker, New York, 1998), Chap. 11
Outlook for 157-nm Resist Design	R. R. Kunz T. M. Bloomstein D. E. Hardy D. K. Downs J. E. Curtin	<i>Proc. SPIE</i> 3678 , 13 (1999)
Outlook for Resist Design at 157-nm	R. R. Kunz T. M. Bloomstein D. E. Hardy R. B. Goodman D. K. Downs J. E. Curtin	<i>J. Photopolym. Sci. Technol.</i> 12 , 561 (1999)
Performance of a Phase-Shift Focus Monitor Reticle Designed for 193-nm Use	R. R. Kunz M. S. Chan* S. P. Doran	<i>Proc. SPIE</i> 3679 , 108 (1999)

*Author not at Lincoln Laboratory.

Long-Term 193-nm Laser Induced
Degradation of Fused Silica and
Calcium Fluoride

V. Liberman
M. Rothschild
J. H. C. Sedlacek
R. S. Uttaro
A. K. Bates
C. VanPeski

Proc. SPIE 3679, 1137
(1999)

Intrapixel Response Test System for
Multispectral Characterization

T. A. Lind
R. K. Reich
W. H. McGonagle
B. B. Kosicki

Proc. SPIE 3649, 232
(1999)

A New RTD-FET Logic Family

R. H. Mathews
J. P. Sage
T. C. L. G. Sollner
S. D. Calawa
C.-L. Chen
L. J. Mahoney
P. A. Maki
K. M. Molvar

Proc. IEEE 87, 596 (1999)

Mechanical Distortions in Advanced
Optical Reticles

A. R. Mikkelsen*
R. L. Engelstad*
E. G. Lovell*
T. M. Bloomstein
M. E. Mason*

Proc. SPIE 3676, 744 (1999)

Metrology Methods for Quantifying
Edge Roughness II

C. M. Nelson
S. C. Palmateer
A. R. Forte
S. G. Cann
S. Deneault
T. M. Lyszczarz

Proc. SPIE 3677, 53
(1999)

*Author not at Lincoln Laboratory.

Resistive Arc Protection for Field-Emitter-Array Cold Cathodes Used in X-Band Inductive Output Amplifiers

L. Parameswaran
C. T. Harris
C. A. Graves
R. A. Murphy
M. A. Hollis

J. Vac. Sci. Technol. B
17, 773 (1999)

Wet Thermal Oxidation of GaN

E. D. Readinger*
S. D. Wolter*
D. L. Waltemyer*
J. M. DeLucca*
S. E. Mohnney*
B. I. Prenitzer*
L. A. Giannuzzi*
R. J. Molnar

J. Electron. Mater. **28**, 257
(1999)

Annealing Studies on GaN Hydride Vapor Phase Epitaxial Layers

D. C. Reynolds*
D. C. Look*
T. Wille*
K. K. Bajaj*
T. C. Collins*
R. J. Molnar

Solid State Commun.
109, 683 (1999)

Approaches to Designing Thermally Stable Schottky Contacts to *n*-GaN

H. S. Venugopalan*
S. E. Mohnney*
J. M. DeLucca*
R. J. Molnar

Semicond. Sci. Technol.
14, 757 (1999)

A Photomixer Local Oscillator for a 630-GHz Heterodyne Receiver

S. Verghese
E. K. Duerr
K. A. McIntosh
S. M. Duffy
S. D. Calawa
C-Y. E. Tong*
R. Kimberk*
R. Blundell*

IEEE Microw. Guid. Wave Lett. **9**, 245 (1999)

*Author not at Lincoln Laboratory.

Thermal Coefficients of the
Expansion and Refractive Index
in YAG

R. Wynne
J. L. Daneu
T. Y. Fan

Appl. Opt. **38**, 3282 (1999)

Rapid Evaluation of Dislocation
Densities in *n*-Type GaN Films Using
Photoenhanced Wet Etching

C. Youtsey*
L. T. Romano*
R. J. Molnar
I. Adesida*

Appl. Phys. Lett. **74**, 3537
(1999)

Mid- and High-Power Passively
Q-Switched Microchip Lasers

J. J. Zayhowski
C. Dill III
C. C. Cook
J. L. Daneu

*Trends in Optics and
Photonics Series*,
M. M. Fejer, H. Injeyan, and
U. Keller, eds. (Optical
Society of America,
Washington, D.C., 1999)

ACCEPTED FOR PUBLICATION

Large-Area Interdigitated Array
Microelectrodes for
Electromechanical Sensing

R. R. Kunz
A. E. Cohen

Sensors Actuators B

Preparation of Silicon-on-Gallium
Arsenide Wafers for Monolithic
Optoelectronic Integration

J. M. London*
A. H. Loomis
J. F. Ahadian*
C. G. Fonstad, Jr.*

Appl. Phys. Lett.

Passively *Q*-Switched Nd:YAG
Microchip Lasers and Applications

J. J. Zayhowski

J. Alloys Compounds

*Author not at Lincoln Laboratory.

PRESENTATIONS[†]

High-Power, High-Brightness 2- μ m
Diode Laser Array

H. K. Choi
J. N. Walpole
A. Sanchez
L. J. Missaggia
Z. L. Liao
G. W. Turner
M. K. Connors
M. J. Manfra
C. C. Cook
D. L. Spears

Diode Laser Technology
Review,
Ft. Walton Beach, Florida,
11-13 May 1999

Laser Beam Combining for Power
and Brightness Scaling

T. Y. Fan
A. Sanchez
C. C. Cook

Diode Laser Technology
Review,
Ft. Walton Beach, Florida,
11-13 May 1999

Multi-spectral Semiconductor Laser
Source for IR-Countermeasures

A. Sanchez
H. Q. Le*
S. Buchter
J. Ochoa
V. Daneu
C. C. Cook
T. Y. Fan
G. Turner
H. Choi
J. Walpole
Z. L. Liao
D. L. Spears
B. Hoden*
K. Hazlett*
T. Crow*
F. Way*

Diode Laser Technology
Review,
Ft. Walton Beach, Florida,
11-13 May 1999

*Author not at Lincoln Laboratory.

[†]Titles of presentations are listed for information only. No copies are available for distribution.

Patterned Contacts for Improved
Beam Stability of 1.55- μm Tapered
Lasers

J. N. Walpole
J. P. Donnelly
L. J. Missaggia
S. H. Groves
P. J. Taylor
S. R. Chinn

Diode Laser Technology
Review,
Ft. Walton Beach, Florida,
11-13 May 1999

AlGaInAs/InP Lasers at 1.55 μm

J. N. Walpole
L. J. Missaggia
C. T. Harris
G. A. Evans*
J. B. Kirk*
T. M. Chou*

Diode Laser Technology
Review,
Ft. Walton Beach, Florida,
11-13 May 1999

Low-Light-Level 640 \times 480-Pixel
CCD Camera for Night Vision Appli-
cations

R. K. Reich
B. E. Burke
W. H. McGonagle

14th Night Operations
Symposium,
Reno, Nevada,
17-20 May 1999

Step Structures of GaInAsSb Grown
on Vicinal Substrates by OMVPE

C. A. Wang
D. C. Oakley

9th Biennial Workshop on
Organometallic Vapor Phase
Epitaxy,
Ponte Vedra Beach, Florida,
23-27 May 1999

Efficient Room Temperature
Cascade Laser Action at 1.4 μm and
3.9 μm in Ho:BaY₂F₈

S. Buchter
A. M. Tabirian*
H. P. Jenssen*
A. Cassanho*
H. Hoffman*

1999 Conference on Lasers
and Electro-Optics,
Baltimore, Maryland,
23-28 May 1999

Nd⁺³ versus Yb⁺³ Solid-State Lasers
at 1 Micron

T. Y. Fan

1999 Conference on Lasers
and Electro-Optics,
Baltimore, Maryland,
23-28 May 1999

*Author not at Lincoln Laboratory.

Outlook for Resist Design at 157 nm	R. R. Kunz T. M. Bloomstein T. H. Fedynyshyn	43rd International Conference on Electron, Ion, and Photon Beam Technology and Nanofabrication Symposium, Marco Island, Florida, 1-4 June 1999
Outgassing of Organic Vapors from 193-nm Photoresists: Impact on Atmospheric Purity Near the Lens Optics	R. R. Kunz D. K. Downs V. Liberman R. S. Uttaro	43rd International Conference on Electron, Ion, and Photon Beam Technology and Nanofabrication Symposium, Marco Island, Florida, 1-4 June 1999
Materials Issues for Optical Component and Photomasks in 157-nm Lithography	V. Liberman M. Rothschild J. H. C. Sedlacek R. S. Uttaro A. K. Bates C. VanPeski T. M. Bloomstein	43rd International Conference on Electron, Ion, and Photon Beam Technology and Nanofabrication Symposium, Marco Island, Florida, 1-4 June 1999
157 nm: The Deepest Deep-UV Yet	M. Rothschild	43rd International Conference on Electron, Ion, and Photon Beam Technology and Nanofabrication Symposium, Marco Island, Florida, 1-4 June 1999
Passively <i>Q</i> -Switched Microchip Lasers and Applications	J. J. Zayhowski	MIT Technology Breakfast Series, Cambridge, Massachusetts, 2 June 1999

Low k1 Lithography for CMOS
Circuits Using Strong Phase-Shift
Methods

M. Fritze

1999 Advanced Reticle
Symposium,
San Jose, California,
8 June 1999

High Frequency Performance of a
Fully Depleted 0.25- μ m SOI CMOS
Technology

D. D. Rathman
J. A. Burns
C-L. Chen
R. Berger
A. M. Soares
R. H. Mathews

1999 IEEE MTT-S
International Microwave
Symposium,
Anaheim, California,
13-19 June 1999

Low Power Electronic Technology
for Portable Devices

J. Burns
C. L. Chen

Optoelectronics Industry
Development Association
Workshop: Advanced
Imaging,
Washington, D.C.,
16-17 June 1999

Advanced Imaging Technology
for Low-Light-Level Sensors

E. D. Savoye

Optoelectronics Industry
Development Association
Workshop: Advanced
Imaging,
Washington, D.C.,
16-17 June 1999

CANARY (Cellular Analysis and
Notification of Antigen Risks and
Yields) Biosensor

T. H. Rider
M. S. Petrovick
A. M. Young
L. T. Smith
R. H. Mathews
S. T. Palmacci
M. A. Hollis

NASA/NCI Biomedical
Imaging Symposium,
Bethesda, Maryland,
25-26 June 1999

Passively *Q*-Switched Nd:YAG
Microchip Lasers and Applications

J. J. Zayhowski

22nd Rare Earth Research
Conference, Argonne
National Laboratory,
Argonne, Illinois,
10-15 July 1999

Demonstration Chips for
PETAFL0P Computers

K. Berggren

6th Hybrid Technology
Multithreaded Project
Workshop,
Annapolis, Maryland,
28-30 July 1999

Tunability Potential for HTS Filters
Using Ferromagnetic Materials

D. E. Oates

Advanced Multifunction
RF Systems Workshop,
Rosslyn, Virginia,
29-30 July 1999

ORGANIZATION

SOLID STATE DIVISION

D. C. Shaver, *Head*
R. W. Ralston, *Associate Head*
N. L. DeMeo, Jr., *Assistant*
Z. J. Lemnios, *Senior Staff*

J. W. Caunt, *Assistant Staff*
K. J. Challberg, *Administrative Staff*
J. D. Pendergast, *Administrative Staff*

SUBMICROMETER TECHNOLOGY

M. Rothschild, *Leader*
T. M. Lyszcza, *Assistant Leader*
T. H. Fedynyshyn, *Senior Staff*
R. R. Kunz, *Senior Staff*

QUANTUM ELECTRONICS

A. Sanchez-Rubio, *Leader*
T. Y. Fan, *Assistant Leader*
T. H. Jeys, *Senior Staff*

Astolfi, D. K.
Bloomstein, T. M.
Craig, D. M.
DiNatale, W. F.
Doran, S. P.
Efremow, N. N., Jr.
Forte, A. R.
Geis, M. W.

Goodman, R. B.
Krohn, K. E.
Lieberman, V.
Maki, P. A.
Palmacci, S. T.
Palmateer, S. C.
Sedlacek, J. H. C.
Uttaro, R. S.

Aggarwal, R. L.
Buchter, S. C.
Cook, C. C.
Daneu, J. L.
Daneu, V.

DiCecca, S.
Goyal, A. K.
O'Brien, P. W.
Ochoa, J. R.
Zayhowski, J. J.

ELECTRO-OPTICAL MATERIALS AND DEVICES

J. C. Twichell, *Leader*
D. L. Spears, *Assistant Leader**
G. W. Turner, *Assistant Leader*
H. K. Choi, *Senior Staff*
R. C. Williamson, *Senior Staff*

Bailey, R. J.
Betts, G. E.
Calawa, A. R.*
Calawa, D. R.
Calawa, S. D.
Connors, M. K.
Donnelly, J. P.
Goodhue, W. D.
Harman, T. C.
Harris, C. T.

Juodawlkis, P. W.
Liau, Z. L.
Lightfoot, A.
Mahoney, L. J.
Manfra, M. J.
McIntosh, K. A.
Missaggia, L. J.
Molnar, R. J.
Mull, D. E.
Napoleone, A.

Nitishin, P. M.
Oakley, D. C.
O'Donnell, F. J.
Poillucci, R. J.
Reeder, R. E.
Taylor, P. J.
Verghese, S.
Walpole, J. N.
Wang, C. A.
Wasserman, J. L.

*Part Time

BIOSENSOR AND MOLECULAR TECHNOLOGIES

M. A. Hollis, *Leader*

Graves, C. A.	Petrovick, M. S.
Mathews, R. H.	Rider, T. H.
Parameswaran, L.	Young, A. M.

ANALOG DEVICE TECHNOLOGY

T. C. L. G. Sollner, *Leader*
L. M. Johnson, *Assistant Leader*
A. C. Anderson, *Senior Staff*

Ala'ilima, T. F.	Oates, D. E.
Berggren, K. K.	Paul, S. A.
Boisvert, R. R.	Sage, J. P.
Feld, D. A.	Santiago, D. D.
Fitch, G. L.	Seaver, M. M.
Holtham, J. H.	Slattery, R. L.
Lyons, W. G.	Weir, T. J.
Macedo, E. M., Jr.	Whittington, R. H.
Murphy, P. G.	

MICROELECTRONICS

B. B. Kosicki, *Leader*
R. K. Reich, *Assistant Leader*
B. E. Burke, *Senior Staff*

Aull, B. F.	Lind, T. A.
Cooper, M. J.	Loomis, A. H.
Daniels, P. J.	McGonagle, W. H.
Doherty, C. L., Jr.	O'Mara, D. M.
Dolat, V. S.	Percival, K. A.
Felton, B. J.	Rathman, D. D.
Gregory, J. A.	Young, D. J.
Johnson, K. F.	

ADVANCED SILICON TECHNOLOGY

C. L. Keast, *Leader*
P. W. Wyatt, *Associate Leader*

Berger, R.	Newcomb, K. L.
Bozler, C. O.	Rabe, S.
Burns, J. A.	Reinold, J. H., Jr.
Chen, C. K.	Sexton, S. V.
Chen, C. L.	Soares, A. M.
Davis, P. V.	Suntharalingam, V.
D'Onofrio, R. P.	Travis, L.
Frankel, R. S.	Tyrrell, B. M.
Fritze, M.	Yost, D.-R.
Gouker, P. M.	Young, G. R.
Knecht, J. M.	

1. QUANTUM ELECTRONICS

1.1 PASSIVELY *Q*-SWITCHED 214.8-nm Nd:YAG/Cr⁴⁺:YAG MICROCHIP-LASER SYSTEM FOR THE DETECTION OF NO

The detection of NO is of interest for a variety of reasons including pollution monitoring, the detection of explosives, and the understanding of atmospheric physics. One technique for detecting NO is laser-induced fluorescence, where the excitation source is tuned to an absorption line of NO in the near uv. For many of the applications listed above, it is desirable to have a system that is compact, robust, portable, low power, and inexpensive, and will operate over a large range of ambient conditions. For a laser-based system, all of these requirements must be satisfied by the excitation source. Passively *Q*-switched Nd:YAG/Cr⁴⁺:YAG microchip lasers meet all of these requirements and provide all-solid-state sources of coherent, subnanosecond, multikilowatt pulses at high repetition rates [1]–[7].

Prior to this report, all of the passively *Q*-switched Nd:YAG/Cr⁴⁺:YAG microchip lasers had been operated at 1.064 μm or 946 nm. The harmonics of these sources do not overlap the NO absorption bands and are not useful for NO detection. It is possible to use a combination of parametric processes and harmonic conversion to get a useful wavelength [4]–[9], but this results in a more complicated device with reduced power and wavelength stability. Nd:YAG has a gain peak at 1.074 μm , whose fifth harmonic, at 214.8 nm, falls within the NO absorption bands. A frequency-quintupled passively *Q*-switched Nd:YAG/Cr⁴⁺:YAG microchip laser operating at this wavelength provides a compact, robust source to use for the measurement of NO. The main challenge in building such a source is the close proximity of the dominant 1.064- μm gain peak, whose effective gain cross section is about twice as large [10]. In the microchip laser there are no intracavity frequency selective elements that can be used to discriminate between the two lines; all of the discrimination must be done with the laser mirror coatings. For the intended application, the laser must operate over a range of temperatures and humidities, placing additional requirements on the coatings.

In the remainder of this report, we briefly discuss the operation of passively *Q*-switched microchip lasers and derive a set of coating requirements for a 1.074- μm device. We then discuss how we meet these challenging requirements to produce an extremely robust 214.8-nm fifth-harmonic system capable of detecting NO at the few-parts-per-billion level.

The principle behind the operation of a passively *Q*-switched laser is that an intracavity saturable absorber prevents the onset of lasing until the average inversion density within the cavity reaches a critical threshold value. The onset of lasing, at that point, produces a high intracavity optical field that saturates the saturable component of the optical loss, increasing the cavity *Q* and resulting in a *Q*-switched output pulse. In their simplest embodiment, the passively *Q*-switched microchip lasers developed at MIT Lincoln Laboratory are constructed by diffusion bonding a thin, flat wafer of Nd:YAG gain medium to a similar wafer of Cr⁴⁺:YAG saturable absorber. The composite structure is polished flat and parallel on the two faces normal

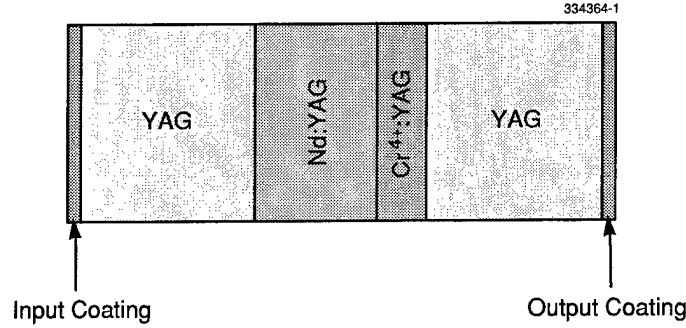


Figure 1-1. Schematic of 1.074- μm passively Q -switched microchip laser.

to the optic axis. Cavity mirrors are deposited directly onto the polished faces. The laser is completed by dicing the wafer into small squares, typically 2 mm on a side. The YAG cavity is mounted on a heatsink and longitudinally pumped with a diode laser. The simplicity of the passively Q -switched microchip laser and its small amount of material give it the potential for inexpensive mass production; nearly monolithic construction results in robust devices.

A schematic of the 1.074- μm passively Q -switched microchip laser is shown in Figure 1-1. The laser consists of 2 mm of undoped YAG, 1.5 mm of Nd:YAG, 0.6 mm of Cr^{4+} :YAG, and 2 mm of undoped YAG, diffusion bonded to each other in the order listed. The Nd:YAG is doped at 1.1 wt% Nd. The Cr^{4+} :YAG has an unsaturated absorption coefficient of 6 cm^{-1} at both 1.064 and 1.074 μm . The undoped YAG endcaps are used to lengthen the output pulses and improve the damage threshold of the device [4]–[7]. The input coating of the laser must be highly transmitting at the pump wavelength of 808 nm and highly reflecting at the oscillating wavelength. Since there are already dual wavelength requirements on this coating, we perform all of the discrimination against the 1.064- μm Nd transition with the output coating.

The passively Q -switched microchip laser reaches threshold when the inversion density is sufficient to generate round-trip gain that is greater than the unsaturated round-trip loss. In the laser there are two main sources of loss, the intracavity loss due to the presence of the Cr^{4+} :YAG saturable absorber and the transmission of the output coupler. The round-trip loss of an optical beam within the (unsaturated) cavity is

$$L_{\lambda} = 1 - \exp(-2\alpha_{\lambda}l_{\alpha})R_{\lambda} \quad , \quad (1.1)$$

where α_{λ} and R_{λ} are the unsaturated absorption coefficient and reflectivity of the output coupler at wavelength λ , and l_{α} is the length of the saturable absorber. The gain of the active cavity is

$$G_{\lambda} = \exp(2n_{i\lambda}\sigma_{\lambda}l_g) \quad , \quad (1.2)$$

where $n_{i\lambda}$ and σ_{λ} are the inversion density and effective gain cross section at wavelength λ , and l_g is the length of the gain medium. To obtain lasing at 1.074 μm , we must satisfy the condition

$$G_{1.074}(1 - L_{1.074}) = 1 . \quad (1.3)$$

To suppress lasing at 1.064 μm ,

$$G_{1.064}(1 - L_{1.064}) < 1 . \quad (1.4)$$

Optimal performance of a passively Q -switched Nd:YAG/Cr⁴⁺:YAG microchip laser is obtained for [11]

$$R_{1.074} \approx \exp(-\alpha_{1.074} l_\alpha) . \quad (1.5)$$

Since, for Cr⁴⁺:YAG, $\alpha_{1.064} \sim \alpha_{1.074}$ and $n_{i1.064} \sim n_{i1.074}$, suppression of oscillation at 1.064 μm requires

$$R_{1.064} < (R_{1.074})^\xi , \quad (1.6)$$

where

$$\xi = 3 \left(\frac{\sigma_{1.064}}{\sigma_{1.074}} \right) - 2 . \quad (1.7)$$

For Nd:YAG, $\sigma_{1.064} \sim 2\sigma_{1.074}$, requiring that $R_{1.064} < (R_{1.074})^4$.

The optical coatings for the microchip laser were produced using an electron-beam evaporation system equipped with a single-rotation semi-spherical substrate holder and 6-kW quartz substrate heaters. The system has an ion-assisted-deposition (IAD) capability that uses a 5-A end-Hall ion source with typical ion energies of 80–120 eV.

The pump-side coating on the microchip laser has a nominal specification of <5% reflectivity at 808 nm and >99.9% reflectivity at 1.074 μm . The output coating is specified to have <5% reflectivity at 1.064 μm and $70 \pm 5\%$ reflectivity at 1.074 μm . The output coating specifications are somewhat more severe than the above derivation indicates, reflecting a large uncertainty in the ratio of the emission cross sections at 1.064 and 1.074 μm .

For the input coating, we used a 21-layer edge-filter design, giving >99.9% reflectivity at both 1.064 and 1.074 μm and typically <1% reflectivity at 808 nm. The enhanced spectral stability associated with IAD techniques was not required for this coating, but the IAD process was used to give a higher damage threshold.

The output coupler used a 21-layer quarter-wave stack followed by a half-wave low-index layer. The design has a very steep skirt on the short-wavelength end of the high-reflectance band, as shown in Figure 1-2, giving the required discrimination between the 1.074- and 1.064- μm lines (<1% reflectivity at 1.064 μm and 70% reflectivity at 1.074 μm , theoretical). This translates into a steepness of $\sim 7\%/nm$. In order to achieve the $\pm 5\%$ reflectivity specification at 1.074 μm , the edge of the high-reflectance band must be positioned within 0.7 nm, or 0.07%, and remain there over the full range of environmental conditions encountered during the operation of the device.

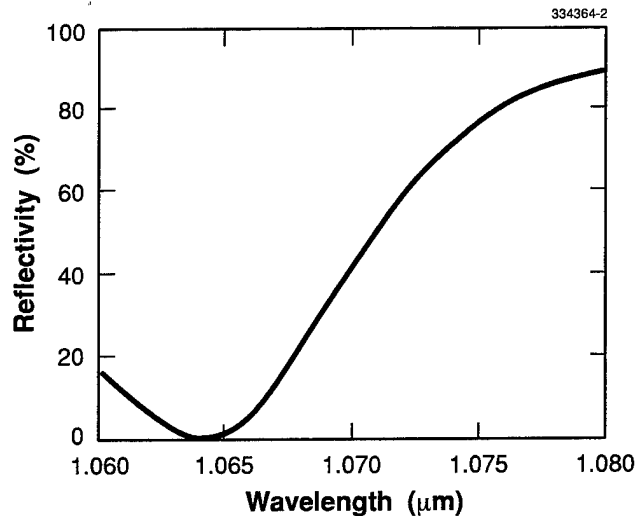


Figure 1-2. Theoretical reflectivity of output coupler.

To achieve the required environmental stability, electron-beam IAD was used in conjunction with an elevated substrate temperature ($\sim 200^{\circ}\text{C}$). The ion source was operated at 0.3 mA/cm^2 (4.5-A anode current) at 100–110 eV (150–160-V anode voltage). This results in a dense film morphology and low porosity to give the coatings a high degree of spectral stability. It also results in high-field-damage-threshold coatings, which we have used on high-power microchip lasers with peak output intensities in excess of 10 GW/cm^2 [4]–[7]. We measured the spectral stability of these coatings to be better than $\pm 0.05\%$ immediately following exposure to a wide range of ambient conditions, including vacuum bake, exposure to 60% humidity for 5 days at room temperature, and immersion in boiling water.

The high accuracy required for the output-coupler coating was achieved by taking advantage of the thickness runoff that normally occurs along the radius of the rotating substrate holder. In-situ optical monitoring allows us to obtain 1% thickness accuracy at a given radial position. Thickness runoff over the radius of the substrate holder is much greater than this. If many substrates are mounted along the radius of the substrate holder, it is possible to adjust their spacing so that at least one has the desired coating properties.

Without any distribution shields, our optical coater has a nearly linear thickness runoff of $\sim 0.6\%$ per radial cm. With a 6.5-cm-wide shield extending radially across the substrate holder, the runoff was reduced to $\pm 1\%$ over a radial distance of 10 cm, as seen in Figure 1-3. Twelve $2 \times 2\text{-mm}$ microchip lasers were positioned radially over this distance, guaranteeing that several of the devices would have coatings meeting the reflectivity specifications.

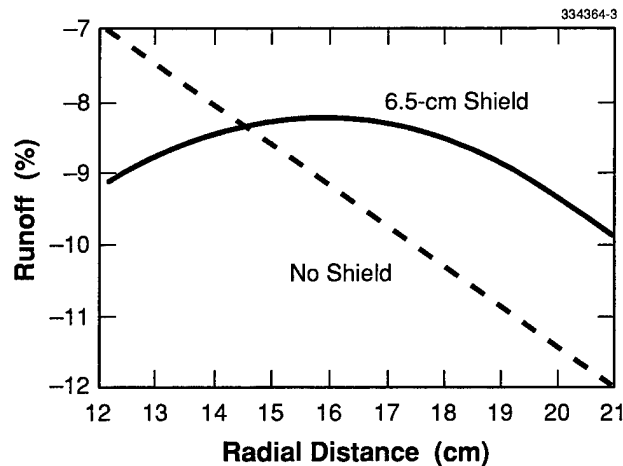


Figure 1-3. Spectral runoff of optical coater with and without 6.5-cm distribution shield.

After coating, the reflectivity of the output surface of each of the microchip lasers was measured at near-normal incidence using a $1.064\text{-}\mu\text{m}$ laser. The reflectivity of witness samples spanning the same radial distances was also measured at both 1.064 and $1.074\text{ }\mu\text{m}$. The results are shown in Figure 1-4, where the microchip lasers have been assigned numbers from 1 to 12, and the measurements of witness samples have been radially collocated with the microchip lasers. The measurements indicated that devices 2–4 and 8–10 should be closest to meeting the coating specifications.

The microchip lasers were longitudinally pumped with the fiber-coupled output of a 12-W diode-laser array. The pump-delivery fiber has a core diameter of $490\text{ }\mu\text{m}$ and a numerical aperture of 0.12. Its output was imaged into the Nd:YAG gain medium with a 0.25 magnification using a pair of aspheric lenses. Pumping was done in a quasi-cw fashion at 1-kHz repetition rate. Devices 2, 4, 5, and 10 were $1.074\text{-}\mu\text{m}$ lasers; devices 3 and 7 failed because of coating damage; the rest of the devices operated at $1.064\text{ }\mu\text{m}$. These results are in general agreement with the spectral measurements and our understanding of the coating requirements (some deviation between the coatings on the microchip lasers and the witness samples is expected).

All of the $1.074\text{-}\mu\text{m}$ microchip lasers have similar properties. When pumped as described above, the minimum pump duration required for the passively Q -switched lasers to produce an output pulse is $120\text{ }\mu\text{s}$. Each of these lasers can be operated at repetition rates up to 2 kHz, and produces an output pulse with a typical pulse energy of $30\text{ }\mu\text{J}$ and duration of 1.6 ns, in a single longitudinal mode with a linearly polarized, $85\text{-}\mu\text{m}$ -radius ($1/e^2$ intensity), diffraction-limited transverse mode.

Device 4 was used to construct a 214.8-nm source. Its output is frequency converted with a set of antireflection-coated nonlinear crystals that was optimized for frequency conversion of a $1.064\text{-}\mu\text{m}$

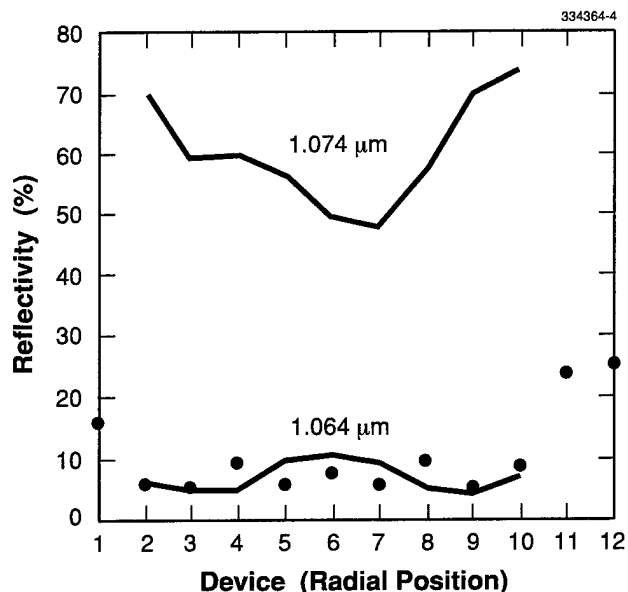


Figure 1-4. Spectral properties of output coatings on 12 microchip lasers (circles) and radially collocated witness samples (lines).

laser [2]–[7]. All of the nonlinear crystals have flat, parallel faces and are butt coupled to each other (and the microchip laser) without any intervening optics. Second-harmonic generation is performed using Type II phase matching in a 5-mm-long piece of KTP, resulting in 8 $\mu\text{J}/\text{pulse}$ of 537-nm light. The slightly lower than expected conversion efficiency is a result of the large angle between the incident light and the normal to the KTP surface ($\sim 14^\circ$, compared to 5° for frequency doubling of 1.064- μm radiation [5]), resulting in greater reflection losses than would be otherwise expected. The output of the KTP is frequency doubled in a 5-mm length of BBO using Type I phase matching. This produces 1.2 $\mu\text{J}/\text{pulse}$ of 268-nm light, which is frequency summed with the fundamental (1.074 μm) using Type I phase matching in a second 5-mm-long piece of BBO. The result is 50 nJ ($\pm 20\%$) of fifth-harmonic light at the desired 214.8-nm wavelength. The entire optical head (fiber-imaging optics, microchip laser, and nonlinear crystals) is packaged in a 2.5-cm-diam \times 8-cm-long stainless steel can, whose only input is the pump-delivery fiber, as seen in Figure 1-5 [4]–[7].

The 214.8-nm output of the frequency-quintupled microchip laser was used to detect NO. The experiment consisted of a flow cell in close proximity to a uv photomultiplier tube. The output of the laser interacted with gas in the flow cell over a useful interaction length of about 1 cm. A 1- σ signal-to-noise level was achieved with a 1-s averaging time for a change in NO concentration of 15 parts per billion in air at atmospheric pressure. The laser was also temperature tuned over the free spectral range of the cavity

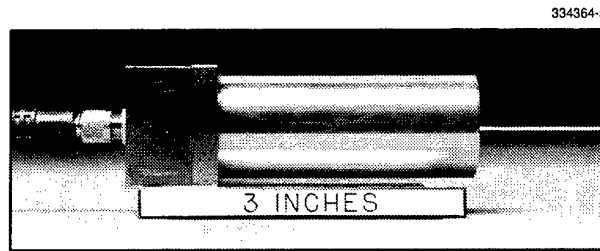


Figure 1-5. Photograph of optical head of 214.8-nm fifth-harmonic microchip laser source.

(13.5 GHz at the fundamental, 67 GHz at the fifth harmonic) to profile 2 of the NO absorption lines at several different pressures. Details of the experiments are reported elsewhere [12].

J. J. Zayhowski
C. C. Cook

REFERENCES

1. J. J. Zayhowski and C. Dill III, *Opt. Lett.* **19**, 1427 (1994).
2. J. J. Zayhowski, *Laser Focus World* **32** (April), 73 (1996).
3. J. J. Zayhowski, *Opt. Lett.* **21**, 588 (1996); errata, **21**, 1618 (1996).
4. J. J. Zayhowski, *Rev. Laser Eng.* **26**, 841 (1998).
5. J. J. Zayhowski, C. Dill III, C. Cook, and J. L. Daneu, in *OSA Trends in Optics and Photonics on Advanced Solid State Lasers*, M. M. Fejer, U. Keller, and H. Injeyan, eds. (Optical Society of America, Washington D.C., 1999), p. 178.
6. J. J. Zayhowski, *Laser Focus World* **35** (August), 129 (1999).
7. J. J. Zayhowski, to be published in *J. Alloys Compounds* (1999).
8. J. J. Zayhowski, *IEEE Photon. Technol. Lett.* **9**, 925 (1997).
9. J. J. Zayhowski, *Opt. Lett.* **22**, 169 (1997).
10. H. G. Danielmeyer, in *Lasers*, A. K. Levine and A. J. DeMaria, eds. (Marcel Dekker, New York, 1976), p. 12.
11. J. J. Degnan and J. J. Zayhowski, "SLR2000 microlaser performance: theory vs. experiment," to be published in *Proceedings of the 11th International Workshop on Laser Ranging*.
12. J. Wormhoudt, J. H. Shorter, and J. J. Zayhowski, to be published in *Appl. Opt.*

2. ELECTRO-OPTICAL MATERIALS AND DEVICES

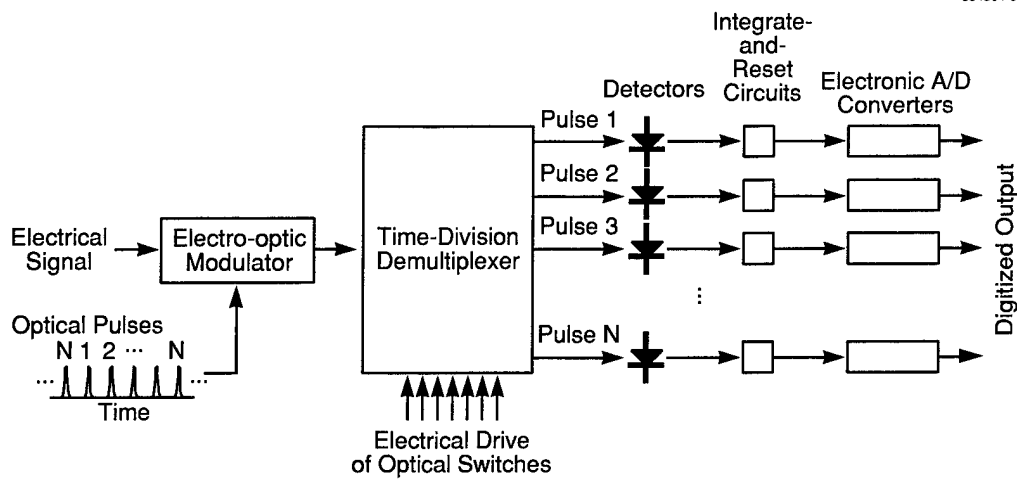
2.1 EFFECTS OF CROSSTALK IN DEMULTIPLEXERS FOR PHOTONIC A/D CONVERTERS

Development efforts are under way for a new generation of high-sampling-rate analog-to-digital (A/D) converters that exploit the unique features provided by optical sampling of electrical signals. These photonic A/D converters utilize a train of optical pulses to sample an electrical input waveform applied to an electro-optic modulator. The resulting train of amplitude-modulated optical pulses is detected and quantized in a conventional A/D converter. This process yields an overall response that can be made highly linear with wide spur-free dynamic range at high sampling rates [1].

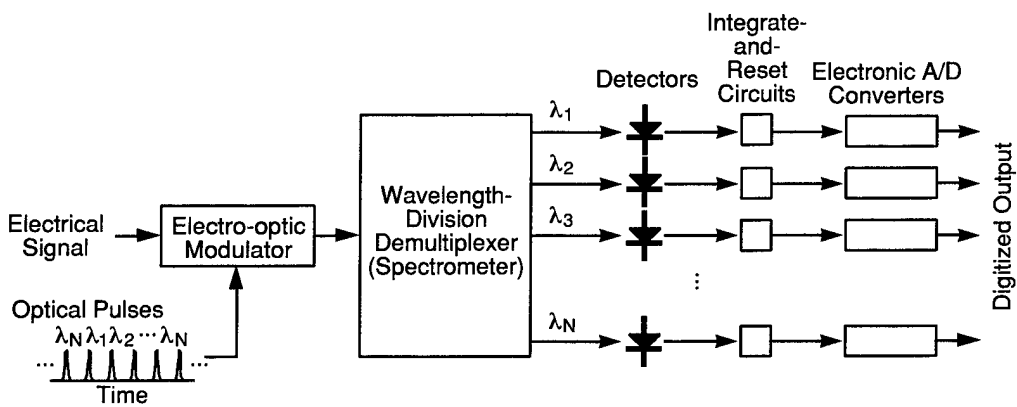
While the linearity and dynamic range of an A/D converter are enhanced by employing optical sampling, the sampling rate is limited by the speed with which the associated electronic A/D converter can quantize the detected optical pulses. An attractive means for increasing the sampling rate by a factor N is to use a $1:N$ demultiplexer at the output of the electro-optic modulator to direct sequential optical pulses to a parallel array of N electrical A/D converters, each operating at a quantization rate of f_s/N where f_s is the sampling rate. Two types of demultiplexing schemes are being explored, time-division demultiplexing [1],[2] and wavelength-division demultiplexing [3],[4], shown schematically in Figure 2-1. As compared to electrical demultiplexers, these optical demultiplexing schemes are attractive because they provide a high-bandwidth highly linear path from the electro-optic modulator to the detectors that retains the analog information in the optical pulses. However, demultiplexing techniques require an extremely precise match of all of the N parallel A/D channels so that digital outputs from these A/D converters can be interleaved to yield a precise representation of the signal sampled at f_s .

In the time-division demultiplexer, shown in Figure 2-1(a), the input pulses are all at the same wavelength. The demultiplexer consists of a cascaded array of electrically driven 1×2 optical switches that direct the sequential optical pulses to the appropriate detectors and electronic A/D converters. In the wavelength-division demultiplexer scheme, shown in Figure 2-1(b), the optical pulses into the modulator occur in groups of N pulses with each pulse in a group at a different wavelength. The demultiplexer is a spectrometer that routes pulses of different wavelengths to different outputs. In both demultiplexing schemes, the possibility exists that there will be incomplete isolation of the different outputs. Crosstalk in the optical switches or in the spectrometer may cause a fraction of the optical pulse representing the sampled electrical signal at one particular time to appear at the wrong output. This crosstalk will cause undesirable spurs in the spectrum obtained by digitally processing the interleaved data from the separate electronic A/D converters. This report analyzes the level of such spurs.

Following each detector in Figure 2-1 is a circuit that must condition the output of the detectors so as to provide a signal that is readily quantized by the associated electronic A/D converter. This conditioning is most readily done by integrating the detector output so as to yield a signal that is essentially constant at the time that the track-and-hold circuit at the input to the electronic A/D converter captures the voltage level



(a)



(b)

Figure 2-1. Photonic analog-to-digital converter systems with optical demultiplexers to increase sampling rate: (a) time-division demultiplexed and (b) wavelength-division demultiplexed systems.

for digitization by the quantizer. After the signal is held, the integrator must be reset to zero in preparation for the next pulse. Any pulse that leaks through during the integration period will be integrated and thus generate errors. In addition, incomplete reset of the integrator will inject an error into the following sample. Therefore, two types of crosstalk can occur: crosstalk in the demultiplexer and incomplete reset of the integrate-and-reset circuit. Both types of crosstalk can generate undesirable spurs.

To analyze the errors due to crosstalk, we express the sampled signal $S(t)$ as the product of the input signal $s(t)$ and a sampling function $w(t)$

$$S(t) = s(t) \times w(t) \quad . \quad (2.1)$$

Ideally, $w(t)$ is a sequence of uniform-amplitude sampling pulses. Errors in $w(t)$ generate spurs in the processed output. Consider a demultiplexer system in which one of the N parallel A/D channels has a gain error. In this case, $w(t)$ will have the form shown in Figure 2-2. For this case, $w(t)$ can be expressed as the sum of a perfect sampling function $W(t)$ and an error function $E(t)$, as shown in Figure 2-3.

The Fourier transform (FT) of the sampled signal $S(t)$ is given by

$$\text{FT} \{S(t)\} = \text{FT} \{s(t) \times [W(t) + E(t)]\} = \text{FT} \{s(t) \times W(t) + s(t) \times E(t)\} \quad (2.2)$$

$$\text{FT} \{S(t)\} = \text{FT} \{s(t)\} * \text{FT} \{W(t)\} + \text{FT} \{s(t)\} * \text{FT} \{E(t)\} \quad , \quad (2.3)$$

where $*$ denotes convolution.

The first term in Equation (2.3) is the desired output and the second term gives the interleaving spurs. For the case in which the input signal is a sinusoid at frequency f_o , the second term yields interleaving spurs around the signal frequency at $f_o + f_s/N$. The relative amplitude of the spurs and the desired signal is given by

$$\text{FT} \{E(t)\} / \text{FT} \{W(t)\} = \epsilon/N \quad (2.4)$$

or

$$\text{Relative spur (dB)} = 20 \log (\epsilon/N) \quad . \quad (2.5)$$

The error signal illustrated in Figures 2-2 and 2-3 is shown as an amplitude error only. With the addition of a crosstalk, the effective time at which a sample is taken is altered because the crosstalk adds in some of a sample taken at a different time. For a sinusoidal input signal, the timing error appears as a phase shift in the weight applied to that sample. The consequences of this leakage and the generalization of Equation (2.5) are derived in this report.

From the foregoing analysis, it is clear that the N parallel A/D channels in a demultiplexed A/D system must be carefully matched in the weights applied to the samples. In order to do this, the gain of each channel must be precisely calibrated so that the quantized output for that channel can be normalized before the samples from the N parallel A/D converters are interleaved. The digitized output $D_n(t)$ of the n th electronic A/D converter associated with an optical pulse sampling the signal $s(t)$ at time t can be expressed in a linear approximation as

$$D_n(t) = A_n + B_n s(t) \quad . \quad (2.6)$$

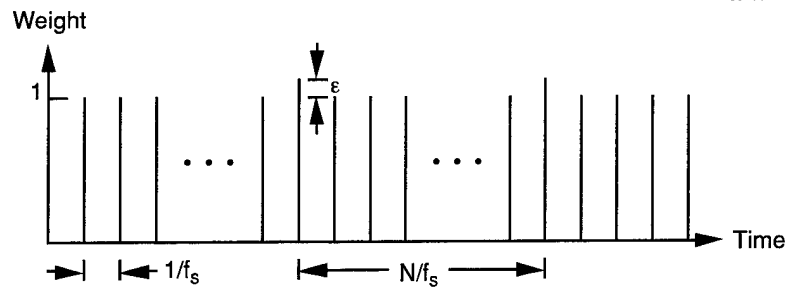


Figure 2-2. Sampling function for capturing an input signal. Sampling rate is f_s and demultiplexing ratio is N . An amplitude weighting error ϵ is shown.

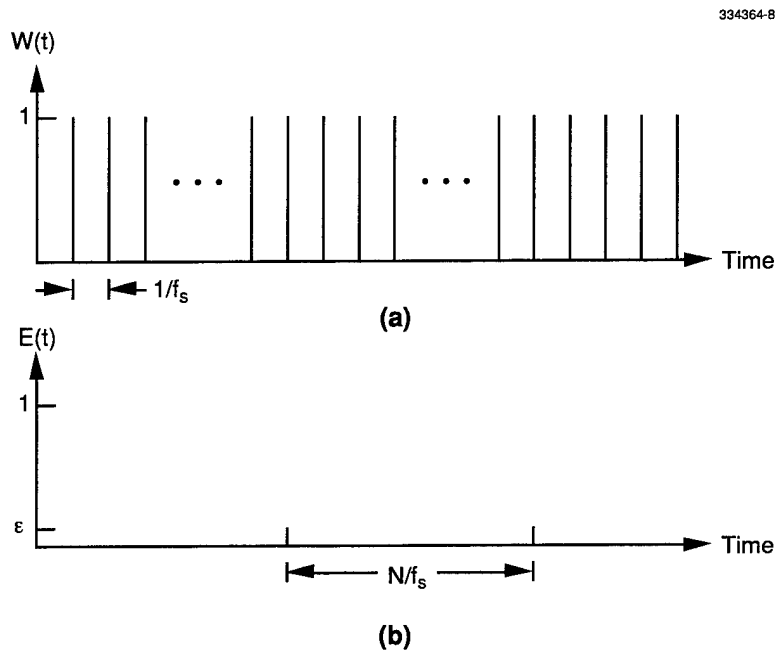


Figure 2-3. Decomposition of time-domain sampling function into (a) a perfect function $W(t)$ and (b) an error function $E(t)$.

In order to extract $s(t)$, the quantities A_n and B_n must be determined through a calibration process. This can be accomplished by making $s(t)$ equal to a low-frequency sinusoid and simultaneously recording the outputs of all of the N parallel electronic A/D converters. Appropriately normalized values of $s(t)$ are obtained by inverting Equation (2.6):

$$s(t) = [D_n(t) - A_n]/B_n \quad (2.7)$$

However, in the presence of crosstalk, this process is imperfect. Consider the case in which some of a pulse representing a sample of the signal at some other time $t - \tau$ leaks into n th A/D converter. In this case,

$$D_n(t) = A_n + A'_n + B_n [s(t) + c s(t - \tau)] \quad (2.8)$$

where A'_n = signal-independent crosstalk and c = relative amplitude of signal-dependent crosstalk.

For a low-frequency calibration signal, $s(t) \approx s(t - \tau)$. The resulting normalized values $s'(t)$ of the signal are given by

$$s'(t) = [D_n(t) - A_n - A'_n]/[B_n (1 + c)] \quad (2.9)$$

However, this normalization leads to errors for high-frequency signals in which $s(t)$ differs significantly from $s(t - \tau)$. Consider the case in which $s(t)$ is a sinusoid at frequency f_o . In this case, Equation (2.8) yields

$$D_n(t) = A_n + A'_n + B_n \{ \sin[2\pi f_o t] + c \sin[2\pi f_o(t - \tau)] \} \quad (2.10)$$

Accordingly, Equation (2.9) yields

$$s'(t) = \{ \sin[2\pi f_o t] + c \sin[2\pi f_o(t - \tau)] \} / (1 + c) \quad (2.11)$$

We will assume that $c \ll 1$ so that terms in Equation (2.11) that scale as c^2 or higher powers can be neglected. With this assumption, the error in measuring $s(t)$ is given by

$$s(t) - s'(t) = c[1 - \cos(2\pi f_o \tau)] \sin(2\pi f_o t) + c \sin(2\pi f_o \tau) \cos(2\pi f_o t) \quad (2.12)$$

Equation (2.12) suggests that the weight given to the samples of the input signal be generalized from the simple amplitude error illustrated in Figures 2-2 and 2-3. For a sinusoidal signal, there is an in-phase error ϵ_r which can be thought of as the real part of the weighting error given by

$$\epsilon_r = c[1 - \cos(2\pi f_o \tau)] \quad (2.13)$$

and an out-of-phase error ϵ_i which can be thought of as the imaginary part of the weighting error

$$\epsilon_i = c \sin(2\pi f_o \tau) \quad (2.14)$$

These results have a geometric interpretation. The weight given to the samples of a sinusoidal signal can be represented as a vector that is the sum of the weight obtained in the absence of crosstalk and a complex error vector as shown in Figure 2-4. The magnitude of the error is given by

$$|\epsilon| = (\epsilon_r^2 + \epsilon_i^2)^{1/2} = |\sin(\pi f_o t)|. \quad (2.15)$$

If there is crosstalk in only one of the N parallel output channels shown in Figure 2-1, then this generalized case yields

$$\text{Relative spur (dB)} = 20 \log(|\epsilon/N|) = 20 \log[2c|\sin(\pi f_o t)|]. \quad (2.16)$$

This equation has several important implications. For the case in which the crosstalk occurs with a time delay of one sample period, $\tau = 1/f_s$ and the interleaving spurs peak at a signal frequency $f_o = f_s/2$ or the Nyquist frequency. If the crosstalk occurs owing to incomplete reset in the integrate-and-reset circuit, then $\tau = N/f_s$ and the interleaving spurs peak at $f_o = f_s/2N$. Measuring the spur level as a function of f_o can identify the source of the crosstalk. Equation (2.16) can be used to identify the value of τ associated with the crosstalk. For demultiplexed photonic A/D converters with large numbers of bits, the tolerable level of crosstalk is quite low. For example, an A/D converter accurate to 12 bits will require $c < 10^{-4}$. This means that the optical demultiplexer must yield optical crosstalk power < -40 dB and the integrate-and-reset circuit must reset to zero to within 10^{-4} of the peak voltage of the electronic A/D converters.

The foregoing analysis is for the simple case of crosstalk at only one value of τ occurring in only one of the N outputs. Straightforward extensions of the analysis accommodate crosstalk in multiple outputs and with multiple values of τ . Also, this simplified analysis assumes a linear electro-optic modulator whose

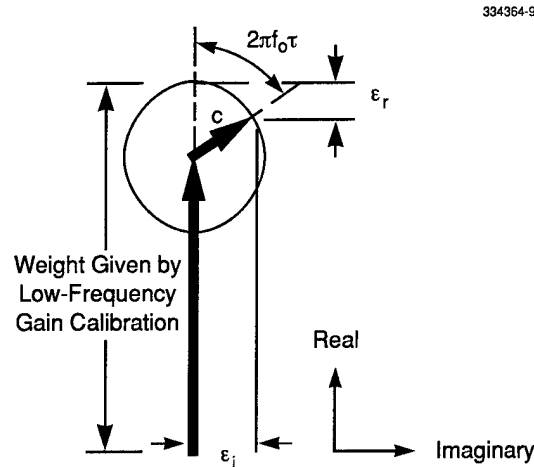


Figure 2-4. Weighting function for one of the parallel channels of a demultiplexed photonic A/D converter system in which there is crosstalk at a level c and a time delay τ . The error is decomposed into an in-phase error ϵ_r and an out-of-phase error ϵ_i .

response is of the form of Equation (2.6). At high levels of the input signal, most modulators are not linear and higher-order terms must be included in Equation (2.6). However, the small-signal approximation used to get the simple result in Equation (2.16) delineates the key mechanisms causing interleaving spurs. The primary effect of higher-level signals will be harmonic responses and third-order intermodulation products, not interleaving spurs.

R. C. Williamson

REFERENCES

1. J. C. Twichell and R. Helkey, Solid State Research Report, Lincoln Laboratory, MIT, 1996:3, p. 28.
2. M. C. Hamilton, J. A. Bell, D. A. Leep, and J. P. Lin, Boeing, private communication.
3. A. S. Bhushan, F. Copinger, and B. Jalali, *Electron. Lett.* **34**, 839 (1998).
4. J. U. Kang, M. Y. Frankel, and R. D. Esman, *IEEE Photon. Technol. Lett.* **10**, 1626 (1998).

3. SUBMICROMETER TECHNOLOGY

3.1 ADVANCED RETICLE FOR 157-nm LITHOGRAPHY

Photolithography with 157-nm F₂ lasers has recently emerged as a serious candidate for the 100- and 70-nm lithography nodes. At this wavelength one must qualify lens materials, reticle substrate materials, and optical coatings. This work, which has its origins in the DARPA-sponsored Advanced Lithography Program, is currently funded under cooperative research and development agreements (CRDAs) with SEMATECH and Intel.

SEMATECH has compiled a list of desired optical material properties for lenses, reticles, and coatings, as presented in Table 3-1. Lenses and coatings are part of the lithography system hardware and as such are expected to have a useful lifetime of many years and may be exposed to high laser fluences. CaF₂ is the leading candidate for lens materials [1]. The study of optical coatings is still in its initial stages.

Reticle materials present a different set of challenges. Good initial transmission needs to be ensured only for a 6-mm thickness of material, and lifetime requirements are not as stringent as those for a lens material because of limited mask utilization. Materials must be prepared with dimensions of 6 × 6 in. and

TABLE 3-1
Optical Materials Targets for 157-nm Lithography*

Component	Initial Target	Lifetime Target	Lifetime Definition
Lens applications	Absorption 0.002/cm, base 10	Absorption 0.003/cm, base 10	10 ¹¹ pulses, 0.5 mJ/cm ² /pulse
Reticles	85% Transmission	84% Transmission	60 × 10 ⁶ pulses, 0.1 mJ/cm ² /pulse
High-reflectance coatings	95% Transmission	Not yet determined	10 ¹¹ pulses, 0.5 mJ/cm ² /pulse
Antireflectance coatings	99% Transmission	98.8% Transmission	10 ¹¹ pulses 0.5 mJ/cm ² /pulse
*As compiled by SEMATECH.			

with excellent transmission uniformity over the full area, and a high degree of parallelism between the faces. Reticles need to undergo a sequence of dry and wet processing steps involved in depositing and patterning absorber layers. Fused silica has been the material of choice for lithography systems operating at 193- and 248-nm wavelengths. Unfortunately, conventional uv-grade fused silica is too opaque when operating at 157 nm.

CaF_2 , LiF and BaF_2 have been evaluated for application as a reticle material. While all these materials satisfy optical transparency and durability requirements for reticle materials, the fluorides have thermal expansion coefficients 40–80 times higher than that of fused silica. The high thermal expansion coefficient can lead to pattern distortion during e-beam mask writing and to image distortion during the wafer exposure through the mask. In fact, recent studies have shown an order-of-magnitude larger distortion of CaF_2 during e-beam patterning compared to fused silica [2],[3].

While conventional fused silica is not transmissive enough at 157 nm, in recent months progress has been made to substantially improve the transmission of fused silica in the wavelength region 155–175 nm. These transmission improvements have been obtained by preparing fused silica with low OH content and by incorporating fluorine into the glass network. These modifications have the effect of moving the absorption edge to shorter wavelengths by eliminating electronic states at the top of the valence band [4]. In Figure 3-1 we show the transmission of conventional uv-grade fused silica and modified fused silica. The transmission of modified fused silica is about 82% at 157 nm, as measured in a vacuum-ultraviolet (VUV)

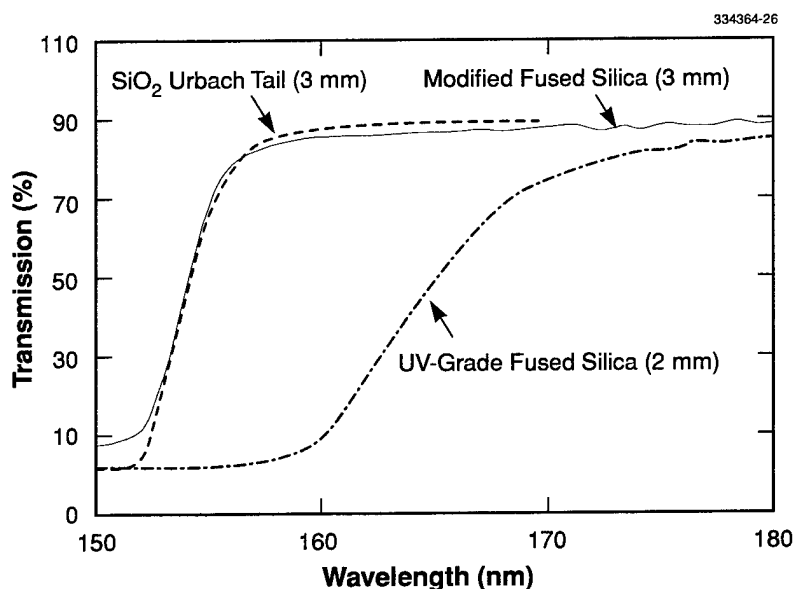


Figure 3-1. Transmission of modified fused silica and uv-grade fused silica in the vacuum-ultraviolet range. The theoretical Urbach tail fit is also shown (see text for details).

TABLE 3-2
Summary of 157-nm Durability Tests for Modified Fused
Silica Material for Reticle Applications*

ID	6-mm Transmission (%)	Pulse Counts Without Degradation (Millions of Pulses)
1	85	>300
2	80.5	80
3	73.5	60
*Incident fluence is 0.1–0.2 mJ/cm ² /pulse. Degradation has been observed at pulse counts larger than those listed.		

spectrometer. We may compare this value to the theoretical maximum of 88%, obtained by allowing for only the Fresnel reflection losses. The actual transmission of this material under laser irradiation can be several percent higher than that in the spectrometer because of laser cleaning of surface adsorbates. In Figure 3-1 we also show a solid line fit to the uv absorption bandedge of modified fused silica, modeled by the Urbach rule as

$$\alpha = \alpha_0 \exp[(E - E_0)s(T)/kT] \quad (3.1)$$

In Equation (3.1), α_0 is the preexponential coefficient, s is a temperature-dependent parameter related to the strength of exciton-phonon coupling, E_0 is approximately equal to the peak in the exciton absorption band, and k is the Boltzmann constant. We obtain a reasonable fit of the modified fused silica absorption cutoff to Equation (3.1) using values of α_0 and s (300 K) from an earlier work on vitreous SiO₂ (Ref. 5) and adjusting E_0 to 8.85 eV as compared to the value of 8.7 ± 0.05 eV in Ref. 5. Note that the model reproduces the sharp transmission cutoff of the modified fused silica quite well, compared to a longer OH-induced absorption tail of the conventional fused silica.

In Table 3-2 we summarize test results for three different grades of fused silica at fluences of 0.1–0.2 mJ/cm²/pulse. We observe that at least one grade of modified fused silica meets the target requirements of SEMATECH for mask materials. For the best grade of fused silica, we can derive a bulk attenuation coefficient of 0.02/cm, base 10 and a loss per each surface of 0.002, base 10. We do observe considerable variations in performance for different grades of fused silica. However, progress is being made by the suppliers, and we expect that improvements in other grades will soon be obtained. We would point out that all the

samples tested so far were relatively small, about 1-in. diameter. Transmission uniformity and durability of reticles over the full 6 × 6-in. area will need to be evaluated in the future.

V. Liberman	R. S. Uttaro
T. M. Bloomstein	A. K. Bates
M. Rothschild	C. Van Peski
J. H. C. Sedlacek	K. Orvek

3.2 VACUUM-ULTRAVIOLET ABSORBANCE OF PHOTORESIST COMPOUNDS

Photolithography using the F₂ excimer laser at 157 nm has been proposed as a bridge between the “traditional” optical lithographies and the “next-generation” lithographies such as extreme ultraviolet (EUV), and has recently been mentioned as a leading candidate for fabrication of devices whose critical dimensions are ~90 nm. Ongoing work to develop EUV (13 nm) lithography has caused researchers to focus on resist-process design to accommodate highly absorbed radiation. Although the challenge to develop a practical, low-defect process for 157 nm seems very similar in many ways, the EUV challenge consists primarily of dealing with ultrathin (<100 nm) resist layers, because development of more transparent materials requires resists with entirely different atomic compositions. However, our work suggests that there is room for innovation in development of new 157-nm materials that does not exist at EUV. This stems from the nature of material absorption throughout the VUV-EUV range. The potential exists for aqueous-base processable photoresists that are 2–3 three times thicker than those proposed for EUV, a difference that may loom important from a defect and yield standpoint. We have measured the VUV absorption of a number of candidate resist materials for 157-nm lithography, with an emphasis on determining which chemical platforms would allow resists to be used at maximum thicknesses while meeting requirements for optical density.

Solid state absorbance of photons in the range 130–180 nm (approximately 7–10 eV) is still dominated by valence band electronic transitions. However, at these higher photon energies, specific chromophores (such as the diazo compounds used at 365 nm) need not be designed into a resist. Rather, many “common” chemical bonds are sufficiently absorptive to lead to efficient excitation of the polymer matrix. Owing to the limited number of VUV spectrophotometers, most structure-property studies of electronic transitions in this regime were performed using either ultraviolet- or x-ray-photoelectron spectroscopies (UPS and XPS, respectively) [6]. A summary of the relevant ground-state electrons as they pertain to photon absorbance at both 13 and 157 nm is shown in Table 3-3 [7]. Very few polymers have had their complete EUV-VUV spectrum published, but polyethylene is one material where this spectrum has been published [8], and it is a good example to show where hydrocarbons undergo their most intense absorption in this region. Figure 3-2 shows the spectrum on a semi-log plot, where one must keep in mind that resists must necessarily contain some oxygen to enable polar solvent solubility. This adds additional absorption between 10 and 50 nm, as seen in Table 3-3. The key point illustrated by both Table 3-3 and Figure 3-2 is

TABLE 3-3
Summary of Photon Absorption Characteristics of Several Ground State
Electrons as Determined by X-Ray Photoelectron Spectroscopy*

Electron	Chemical Bond Type	Binding Energy (eV)	Band Edge (nm)	EUV	157 nm
C(1s)	Any	282–294	<4.4		
C(2s)	Any	12–25	<100	†	
C(2p)	Any	2–10	Varies		†
	C(2p)-F(2p)	10	<124		†
	C(2p)-H(1s)	7.5	<165		†
	C(2p)-O(2p)	7	<180		†
	C(2p) (benzene)	5.3	<240		†
	C(2p) (anthracene)	2.7	<450		†
	C(2p) (graphite)	2	<600		†
O(2s)	Any	23	<54	†	
F(2s)	Any	30	<41		
F(2p)	Any	10	<124		
*See references 6 and 7. †Indicates which chromophores dominate absorption at the respective wavelengths.					

that the EUV absorbance is dominated by photon absorption caused primarily by the **C(2s)** and **O(2s)** ground state electrons. These transitions are only weakly affected by the chemical bonding environment. However, the 157-nm absorption is dominated by **C(2p)** electrons, whose absorption band edge is very close to 157 nm, and whose transition probability can be dramatically affected by the chemical bonding environment. This means the bonding environment in a carbon-backbone polymer can be manipulated to maximize or reduce 157-nm absorbance.

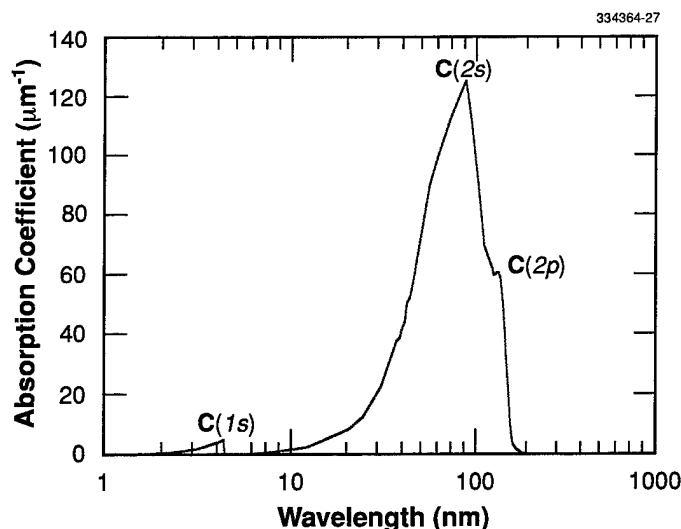


Figure 3-2. Absorbance spectrum for (base e) poly(ethylene) (based on numerical data in Ref. 8).

Our first interest was to determine the absorbance of several classes of commercial resists either in use or under consideration for use in manufacturing. These results are shown in Table 3-4, along with calculations showing how thick each resist would have to be in order to afford an optical density of 0.4, which is considered a typical value. These results clearly demonstrate that, unlike 193 nm, where these particular materials' absorbances differ by 2 orders of magnitude, all these resists have roughly the same absorption coefficient and they would all require thicknesses under 90 nm.

A key element of this study was to make a comprehensive determination of the molecular structure dependence of the absorbance. This was performed by determining the absorption coefficient of over 50 different polymers, of which a partial list is shown in Table 3-5, and by breaking each polymer down into its discrete chromophores. By solving a linear algebraic matrix (one equation for each of the 50 polymers and one variable for each type of chromophore) we were able to develop an analytical approach to estimate absorbances by means of individual group contributions. Not only is this useful for estimating the absorbances of materials not yet synthesized, but it has also illustrated anomalous absorption resulting from things such as high water retention, conformational effects, and electronic delocalization. Based on the understanding provided by this exercise, we now are able to say with greater certainty what the resist options are for 157 nm.

In addition to polymeric resins, we performed measurements on a number of different photoacid generators (PAGs). These measurements were obtained by mixing known quantities of each PAG into a highly transparent ($<0.1 \mu\text{m}^{-1}$) hydrogen silsesquioxane resin, then by determining the absorption coefficient of the resin with and without the PAG. The data are shown for both 157 and 193 nm in Table 3-6, and can be converted to added absorbance by

TABLE 3-4
Summary of Absorption Coefficients and Photon Penetration
Depths Measured for a Variety of Commercially Available Resists*

Resist	A (μm^{-1})	L (OD = 0.40) (nm)	Type of Resist
A	8.7	46	Acrylic
B	8.3	48	Phenolic
C	8.0	50	Acrylic
D	4.6	87	Acrylic
E	5.2	77	Cyclo-olefin
*L is the corresponding thickness of a film with optical density (OD) of 0.4.			

$$A_{\text{PAG}} = \frac{\sigma N f \rho L}{M_w}, \quad (3.2)$$

where σ (cm^2) is the absorption cross section, N (molecules/mole) is Avogadro's number, f is the weight fraction of PAG in the resist, ρ (g/cm^3) is the resist density, L (cm) is the resist thickness, and M_w (g/mole) is the PAG molecular weight. From this, we see that bis(*t*-butylphenyl) iodonium camphor sulfonate, at 3 wt% loading, would increase the absorbance of a 200-nm-thick resist layer by ~0.05, or ~10–15% of the total absorbance. Other PAGs would contribute less.

Interestingly, the absorbances of nearly every PAG are weaker at 157 nm than at 193 nm. This stems from the fact that the aryl $\pi \rightarrow \pi^*$ electronic transition peaks very near 193 nm, and has a much weaker absorption at 157 nm.

From these measurements, we are well on our way to identifying which existing commercial resists will be best suited for the characterization of prototype 157-nm imaging optics in the near term, and developing longer-term plans to prepare new materials that will best meet the manufacturing requirements for 157-nm resists as set forth by the Semiconductor Industry Association.

R. R. Kunz	R. B. Goodman
T. M. Bloomstein	D. K. Downs
D. E. Hardy	J. E. Curtin

TABLE 3-5
Absorption Coefficients A at 157 nm for a Number of Different Polymers

Polymer	A (μm^{-1})	L (OD = 0.4) (nm)
Si-O Backbone:		
Poly(hydrosilsesquioxane)	0.06	6667
Poly(dimethylsiloxane)	1.61	248
Poly(phenylsiloxane)	2.68	149
Carbon Backbone:		
Fluorocarbon, 100% fluorinated	0.70	571
Hydrofluorocarbon, 30% fluorinated	1.34	298
Partially esterified hydrofluorocarbon, 28% fluorinated	2.60	154
Poly(vinyl alcohol) (99.7%)	4.16	96
Fully esterified hydrofluorocarbon, 31% fluorinated	4.56	88
Ethyl cellulose	5.03	80
Poly(methyl methacrylate)	5.69	70
Poly(norbornene)	6.10	66
Polystyrene	6.20	64
Poly(vinyl phenol)	6.25	64
Poly(norbornylmethacrylate)	6.67	60
Poly(adamantylmethacrylate)	6.73	59
Poly(β -pinene)	7.15	56
V1.0 acrylic terpolymer resin	8.20	49
Poly(chlorostyrene)	10.15	39
Poly(vinyl naphthalene)	10.60	38
Poly(acrylic acid)	11.00	36

TABLE 3-6
Absorption Cross Sections Measured at Both 157 and 193 nm for a
Number of Different Photoacid Generator Molecules

Photoacid Generator	$\sigma_{157} \text{ (cm}^2\text{)}$	$\sigma_{193} \text{ (cm}^2\text{)}$
Phthalimido trifluoromethane sulfonate	1.3×10^{-17}	2.0×10^{-17}
Dinitrobenzyl tosylate	1.6×10^{-17}	4.1×10^{-17}
n-decyl disulfone	1.7×10^{-17}	1.8×10^{-17}
Naphthylimido trifluoromethane sulfonate	2.3×10^{-17}	2.3×10^{-17}
Tritolyl sulfonium trifluoromethane sulfonate	3.0×10^{-17}	8.0×10^{-17}
Pyrogallol tris(tosylate)	3.2×10^{-17}	1.3×10^{-16}
Pyrogallol tris(ethane sulfonate)	3.7×10^{-17}	1.0×10^{-16}
Naphthylimido t-butyl benzene sulfonate	4.2×10^{-17}	5.9×10^{-17}
Bis(t-butylphenyl) iodonium camphor sulfonate	6.8×10^{-17}	8.5×10^{-17}

REFERENCES

1. V. Liberman, T. M. Bloomstein, M. Rothschild, J. H. C. Sedlacek, R. S. Uttaro, A. K. Bates, C. Van Peski, and K. Orvek, to be published in *J. Vac. Sci. Technol. B*, 1999.
2. K. Orvek, G. Pugh, J. DeWitt, Y. Korobko, R. Tiberio, D. Carr, R. Sparrow, S. Stevens, J. Gustafson, B. Smith, and A. Bourov, presented at the 157-nm Lithography Workshop (Litchfield, Ariz., 15-17 February 1999), organized by International SEMATECH.
3. J. Chang, A. Abdo, B. Kim, T. M. Bloomstein, R. Engelstad, E. Lovell, W. Beckman, and J. Mitchell, to be published in *Proc. SPIE*, 1999.
4. C. M. Smith and L. A. Moore, to be published in *Proc. SPIE*, 1999.
5. I. T. Godmanis, A. N. Trukhin, and K. Hubner, *Phys. Status Solidi B* **116**, 279 (1983).
6. J. J. Pireaux, J. Riga, R. Caudano, and J. Verbist, "Electronic structure of polymers," in *Photon, Electron, and Ion Probes of Polymer Structure and Properties* (American Chemical Society, Washington, D.C., 1997), p. 169.
7. D. Briggs and M. P. Seah, eds., *Practical Surface Analysis by Auger and X-ray Photoelectron Spectroscopy* (Wiley, New York, 1983).
8. E. D. Palik, ed., *Handbook of Optical Constants of Solids II* (Academic, San Diego, 1991), pp. 657-687.

4. BIOSENSOR AND MOLECULAR TECHNOLOGIES

4.1 NANOPORES FOR DNA SEQUENCING

Deoxyribonucleic acid (DNA) is a complex molecule that contains all of the instructions required to make and maintain a living organism. A DNA molecule consists of two polynucleotide chains composed of four types of nucleotide subunits, or bases. These chains, also referred to as strands, are held together by hydrogen bonds to form a double helix. Specific sequences of nucleotide bases are chemically translated into specific amino acids, which are then joined together to form the protein molecules that control cell structure and function. Thus, we can obtain all of the information required to determine the structure and function of an organism by reading the sequence of bases in a DNA strand. This is driving the considerable effort being expended in projects to sequence the genomes of various organisms, most notably that of humans.

The ability to rapidly sequence DNA molecules will have an enormous impact in a variety of areas including medical applications such as genetic engineering and disease prevention, biological agent identification, and forensics. Current techniques for sequencing DNA consist of using polymerase chain reaction (PCR) to make many copies of each section of DNA, followed by gel electrophoresis to separate and sequence them. These techniques are laborious and time consuming, so much so that at current rates, an estimated 15 years would be required to sequence the entire human genome, which has a length of 3×10^9 bases.

Recently, researchers at Harvard University have developed a technology that has the capability of rapidly sequencing individual bases in single-stranded DNA molecules by measuring ionic current changes as each strand passes through a nanoscale pore sized to admit only a single strand. Measurements of ionic current flow through ion channels in biological membranes are commonly used in biophysics and neurobiology studies. The cell membrane is a typical biological membrane, and is composed of two layers of phospholipid molecules (consisting of a hydrophilic head with a phosphate group, and a hydrophobic hydrocarbon chain tail), in which protein molecules reside, spanning the bilayer. The protein molecules act as ion channels, allowing or blocking the flow of ions between the cell and its environment. Certain large ion channels in lipid bilayer membranes have been shown to remain open for extended time periods, allowing measurements of continuous ionic current flow through the channel. By drawing DNA or ribonucleic acid (RNA) molecules through these channels, the current flow is blocked in a detectable manner, thereby giving an indication of the size of the molecule [1]. The basic technique is illustrated in Figure 4-1(a). Single strands are drawn sequentially through protein channels in a lipid bilayer membrane separating two solution-filled compartments. The negatively charged DNA is pulled through the pore into the positive-ion-filled compartment. Preliminary experiments have been done utilizing lipid bilayer membranes [1], and Figure 4-1(b) shows a measured ionic current trace for a strand with 1060 bases. Ionic current is reduced as the strand passes through the channel. Since the decrease in current is a function of the size of the molecule blocking the channel, it is possible to discriminate between each of the four types of nucleotide bases with a sufficiently precise measurement of the decrease in current as the strand passes through the channel, as schematically shown in Figure 4-1(c).

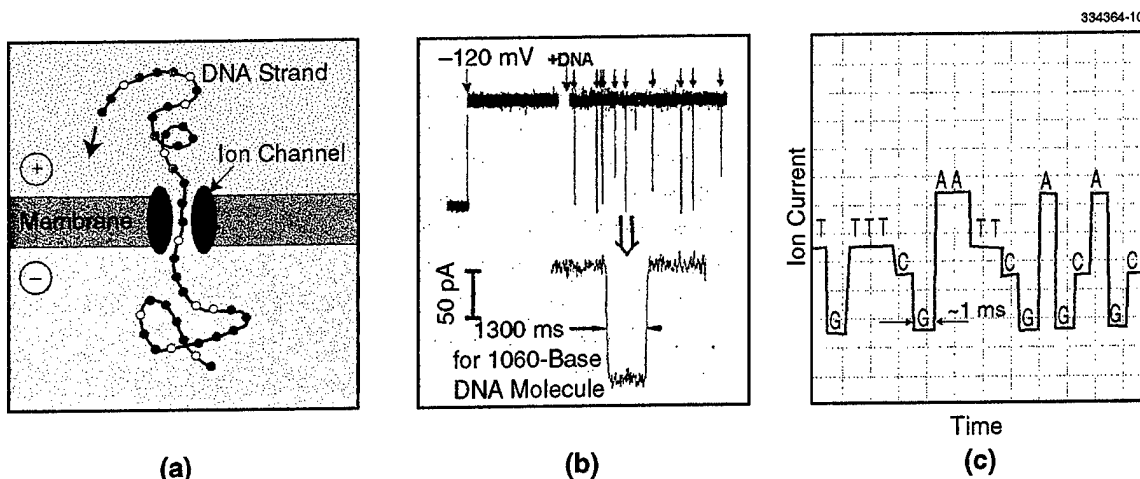


Figure 4-1. (a) Schematic diagram of DNA strand being drawn through ion channel. (b) Measured current trace from DNA strand moving through lipid bilayer membrane. (c) Conceptual schematic diagram of current trace indicating identification of individual bases in DNA strand.

The method makes it potentially possible to sequence entire genomes in very short time periods. For example, using a device with 500 pores, each with a read rate of 1000 bases/sec, a human genome of length 3×10^9 bases can be sequenced in less than 2 h. The high-speed nature of the entire process stems from the fact that the DNA is directly sequenced, without the need for cloning and labeling.

Although the feasibility of the technique has been demonstrated using biological membranes in the form of lipid bilayers, a silicon-based solid state approach can provide the advantages of batch fabrication, precision in pore formation, robustness of the nanopore membranes, and eventually the possibility of integrated readout schemes. In order to use the nanopores for sequencing of individual strands of DNA, they must have a diameter of no more than 30 Å. We have used silicon fabrication techniques to create silicon nitride membranes deposited over precisely defined arrays of etched tips. Each nanopore is formed through the silicon nitride membrane at the apex of a tip. The final opening of the nanopores is done with a novel feedback-controlled reactive ion etch process developed by Professor J. Golovchenko at Harvard University. This technique consists of performing a reactive ion etch of the material while counting ions passing through the etched opening as the etch proceeds. The ion count is a function of the size of the etched pore and can be used to terminate the etch upon reaching a predetermined pore diameter. By using the feedback-controlled etch in the vicinity of a sharp tip, it is possible to open a very small hole (<50 Å) by removing material at the apex of the tip.

Two possible fabrication processes are illustrated in Figures 4-2 and 4-3. Both use conventional optical lithography and anisotropic etching to create precisely defined arrays of silicon features coated with silicon nitride. Bulk anisotropic etching is used to remove the substrate surrounding the silicon nitride thereby forming membranes, and the pores are then opened in the silicon nitride via the feedback-controlled reactive ion etching method. Process 1, shown in Figure 4-2, uses a silicon-on-insulator substrate and relies on a tight control of the top silicon layer thickness for eventual control of the pit dimensions. Process 2, shown in Figure 4-3, uses a conventional silicon substrate, but requires a chemical-mechanical polishing step for planarization of the membrane. As detection of individual bases relies on measurements of very small current levels and changes in current, all surfaces are passivated with dielectric, and high-resistivity substrates are used to minimize leakage currents.

Another option for pore formation (in planar membranes) is the use of direct-write electron-beam lithography, provided a suitably small beam spot size (<50 nm) is available. Alternatively, a composite silicon-organic device can be envisioned, in which the nanopore consists of a protein channel in a small portion of lipid membrane attached to a silicon micropore formed using one of the above two processes. However, our initial approach has been to fabricate a fully silicon-based device using deep-uv lithography for definition of the etched tips or pits, after which the nanopores are opened, as this method has the advantage of simplicity.

An initial set of devices has been fabricated using process 2, with two variations in the tip shape. Figure 4-4 shows scanning electron micrographs of the two tip shapes. The pyramidal shape in Figure 4-4(a) was obtained by using a wet anisotropic etch to form the tip. Conversely, the tip in Figure 4-4(b) was formed using an isotropic plasma etch. This approach, while resulting in a sharper tip and therefore a better chance of minimizing the size of the nanopore, may increase the resistance seen by the fluid and DNA strands flowing through the resulting narrower channel.

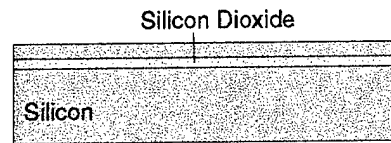
Figure 4-4(c) shows the underside of a completed nitride membrane with its tip-shaped depression, and Figure 4-4(d) is a plan view transmission electron micrograph (TEM) of a completed nanopore with a diameter of 20 nm, produced at Harvard using their feedback-controlled reactive ion etch process. Smaller pores are expected with devices containing isotropically etched tips.

Subsequent versions of the device may incorporate monolithically integrated planar electrodes surrounding the nanopore. These electrodes can be used for measurements of tunneling current into and along the DNA strand as it passes through the pore, providing another means of discrimination of individual bases in the strand.

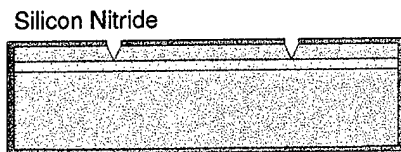
L. Parameswaran
M. A. Hollis

REFERENCE

1. J. J. Kasianowicz, E. Brandin, D. Branton, and D. W. Deamer, *Proc. Natl. Acad. Sci. USA* **93**, 13770 (1996).



Starting substrate:
Silicon-on-insulator (SOI) wafer
(high-resistivity substrate)



1. Deposit silicon nitride etch mask
2. Pattern and etch front side pores
(stop etch when pyramid point
is just above oxide interface)



3. Strip all silicon nitride
4. Deposit thin silicon nitride for pores
and back side etch mask
5. Pattern and etch back side openings



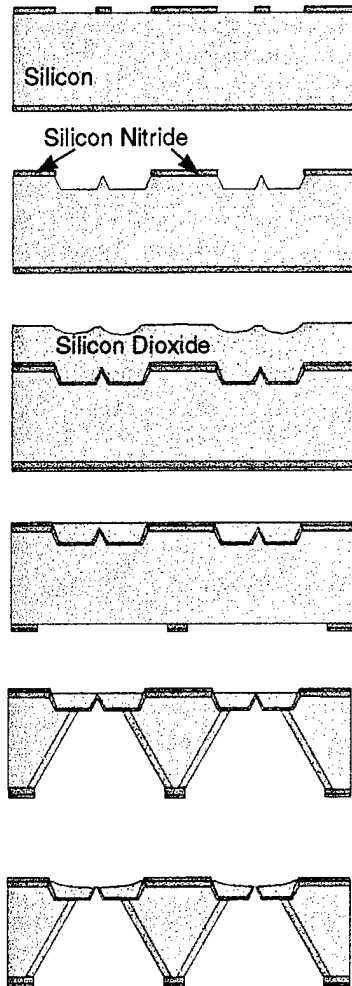
6. Strip all nitride from back side
7. Etch oxide in back side openings
8. Thermally oxidize exposed silicon
in pore region and on sidewalls



9. Open pores with feedback ion etch

Figure 4-2. Fabrication process using a silicon-on-insulator substrate and relying on tight control of the top silicon layer thickness for eventual control of pit dimensions.

Starting substrate: High-resistivity wafer



1. Deposit silicon nitride etch mask
2. Pattern and etch nitride for pyramid etch
3. Etch pyramids and mesas
4. Deposit thin silicon nitride layer
5. Deposit thick oxide over front side
6. Polish oxide and stop on mesa nitride
7. Pattern back side nitride
8. Etch back side openings
9. Oxidize sidewalls of back side openings
10. Remove thin layer of oxide on front to expose nitride tips
11. Open pores with feedback ion etch

Figure 4-3. Fabrication process using a conventional silicon substrate but requiring a chemical-mechanical polishing step to planarize the membrane.

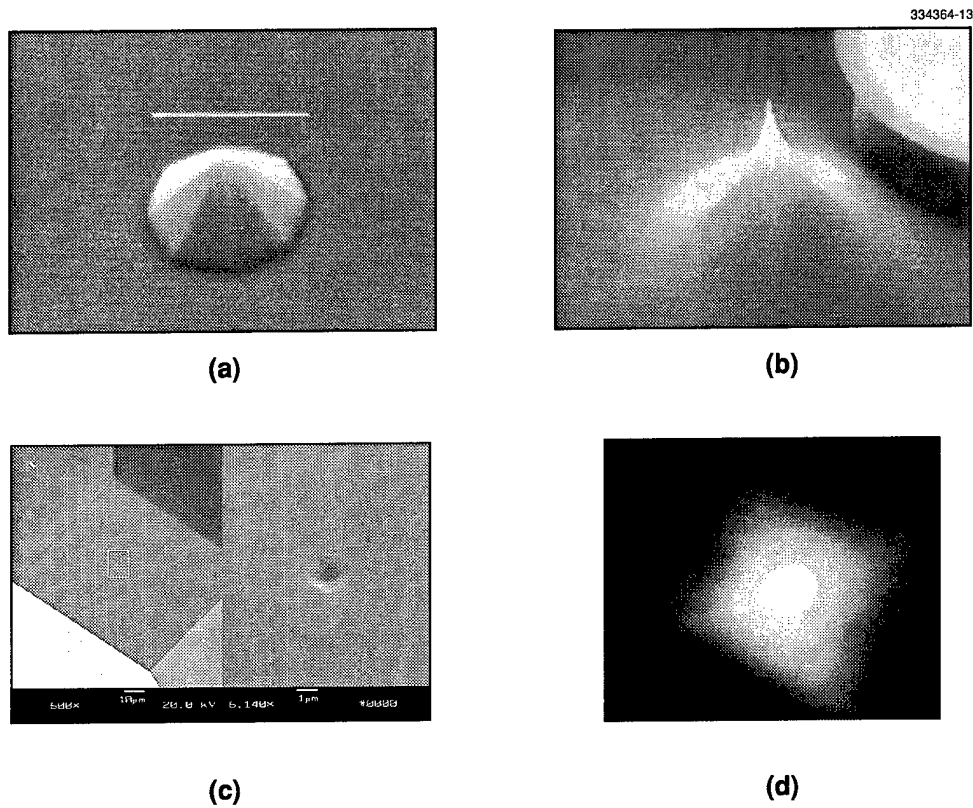


Figure 4-4. (a) Silicon tip formed by wet anisotropic etch; base diameter is 2 μm . (b) Silicon tip formed by isotropic plasma etch; base diameter is 2 μm . (c) Underside of wet-etched tip-shaped depression in silicon nitride membrane, with close-up of tip region. (d) Plan view TEM of completed nanopore with diameter of 20 nm.

5. ADVANCED IMAGING TECHNOLOGY

5.1 BRIDGE BONDING OF GEIGER-MODE AVALANCHE PHOTODIODE ARRAYS TO CMOS TIMING CIRCUITS

Laser and detector technologies are being developed at MIT Lincoln Laboratory that make it possible to build a three-dimensional laser radar (ladar) with several attractive features, including capture of an entire three-dimensional image on a single laser pulse, tens of thousands of pixels, range resolution better than 10 cm, and small size. The laser technology is based on diode-pumped passively *Q*-switched solid state microchip lasers operating at 532-nm wavelength. The detector technology is based on arrays of avalanche photodiodes (APDs) operating in Geiger mode, with integrated timing circuitry for each pixel. We report on a process that has been developed for solving one of the major challenges of this technology—integrating the APD wafers with the CMOS timing circuitry chips.

A common method for attaching a detector array substrate to a silicon read-out integrated circuit (ROIC) substrate is bump bonding. This is appropriate for material combinations, such as InGaAs grown on InP substrates, in which the substrate is optically transparent at wavelengths where the detector is sensitive, allowing back-illuminated operation without the need for substrate removal. In the case of homoepitaxial silicon APDs, however, the substrate is opaque at the wavelength of operation (532 nm), and the APD wafer must be thinned after bump bonding to a thickness of about 10 μm in order to achieve high detection probability. In order to ensure a mechanically sturdy device, therefore, the voids between the bumps must be filled before the thinning operation is carried out. Although filling is straightforward for small arrays, its yield and scalability to larger arrays is uncertain. Therefore, instead of using bump bonding, we have developed a technique that we call bridge bonding. In this method, illustrated in Figure 5-1, void-free mechanical packaging is accomplished by simply epoxying the CMOS chip and the APD wafer face to face. A commercial flip-chip bonding system is used in this step as an alignment and pick-and-place tool. The APD wafer is then thinned for back-illuminated operation. The electrical connections between the APD and CMOS pads are made last by etching sloped vias through the epoxy and patterning a metal connection over that slope (the bridge). The process can either be performed on a wafer-to-wafer basis or a chip-to-wafer basis, since the APD thinning process is a full-wafer process developed for back-illuminated charge-coupled devices. The chip-to-wafer process is favored, since it enables one to bond verified CMOS chips to verified APD arrays.

The photograph in Figure 5-2 demonstrates successful chip-to-wafer bonding followed by wafer thinning using dummy chips and a dummy wafer. In the actual process, after chip bonding and before wafer thinning, a second wafer is epoxied to the chip side for mechanical support. For the experiment depicted in the photograph, a mechanical support wafer was not used. At the outset, a major difficulty was stress-induced device damage caused by contraction of the epoxy used for the support wafer during the curing step. By suitable chemical alteration to soften this epoxy, we have reduced this stress so that no mechanical damage occurs. We can bond several chips to a wafer, attach the mechanical support wafer, cure, and then thin to obtain a collection of sturdy devices.

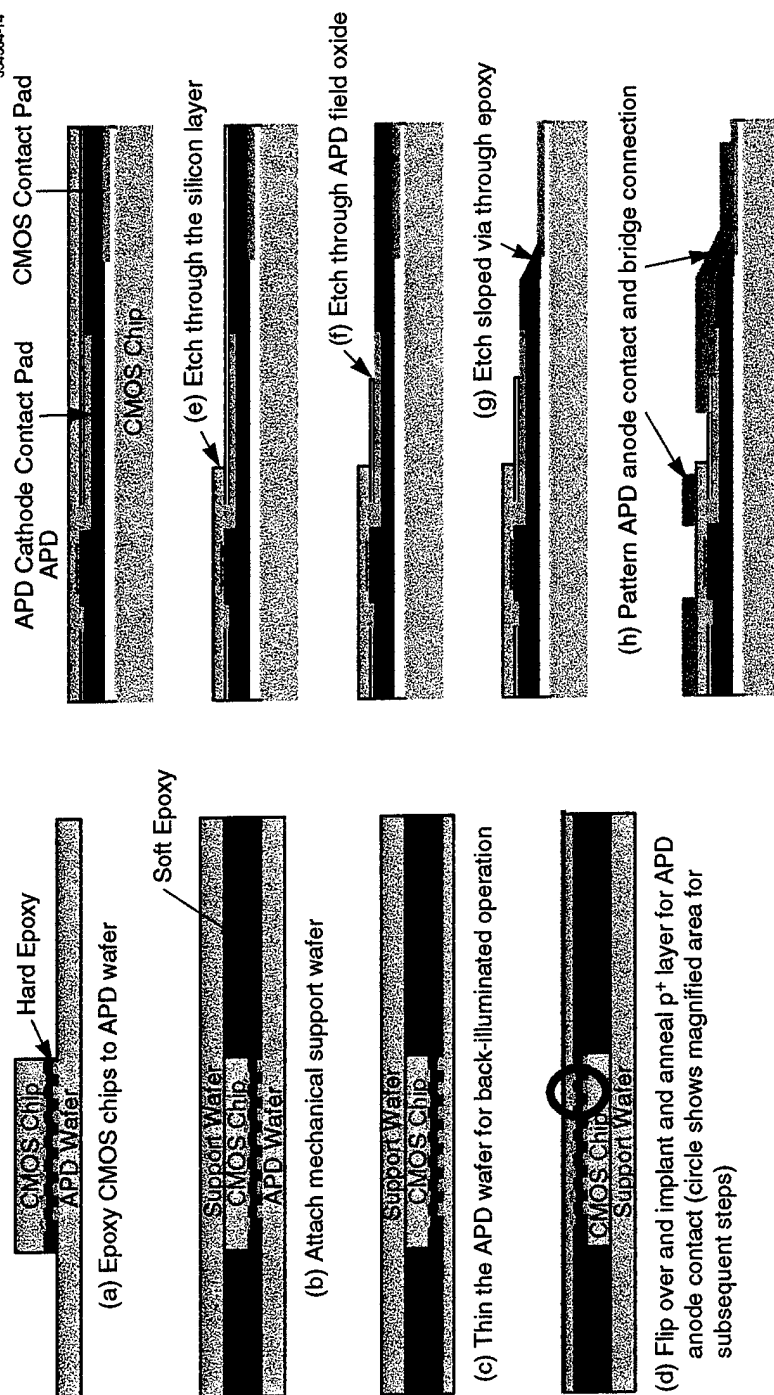


Figure 5-1. Steps in the bridge-bonding process.

Figure 5-3 shows a sloped profile etched in the epoxy used to bond the APDs and CMOS circuits together. The sloped profile is achieved by dry etching, using a photoresist that is etch-rate matched to the epoxy. The ability to etch such a sloped via controllably facilitates patterning of the metal bridge with good step coverage.

The bridge-bonding process was first demonstrated using several dummy CMOS chips epoxied to a dummy APD wafer. These parts consisted of 32×32 arrays of metallization patterns designed to allow direct probing to verify that good electrical connections were made. This initial test device had a nonuniform epoxy thickness across each array, so the epoxy etch time was adjusted to remove the average thickness, causing the epoxy to be overetched in some pixels and underetched in others. Electrical probing showed good electrical connections in 100% of the pixels in which the etch time was sufficient to expose the bond pad on the dummy CMOS chip. The bridge-bonding process was subsequently carried out using real 32×32 ROIC chips and a wafer with real 32×32 APD arrays. Figure 5-4 is a photograph showing the pixels of this device after completion of the bridge-bonding process.

The process should be scalable to larger array sizes, and its demonstration represents an important step toward integrated sensor arrays that support scannerless imaging laser radars.

A. H. Loomis
B. F. Aull

334364-25

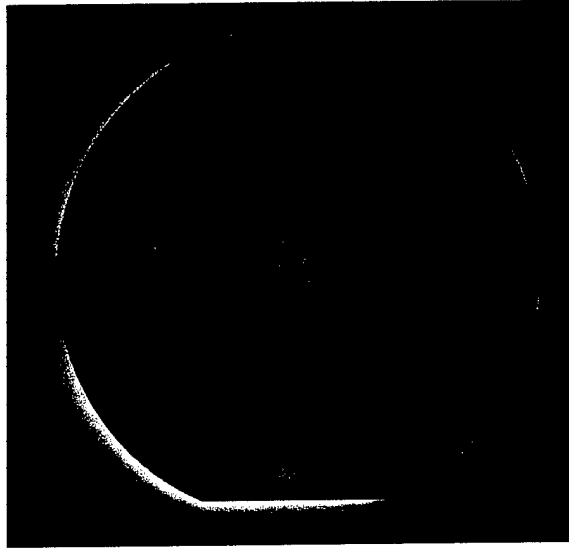


Figure 5-2. Silicon wafer which has had chips bonded to it and then undergone thinning.

334364-15

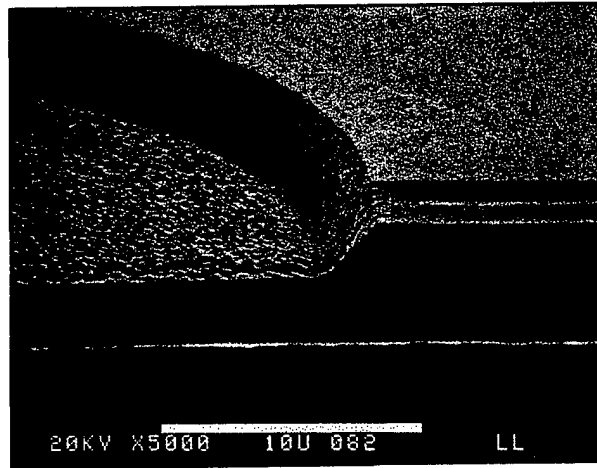


Figure 5-3. Sloped epoxy etch.

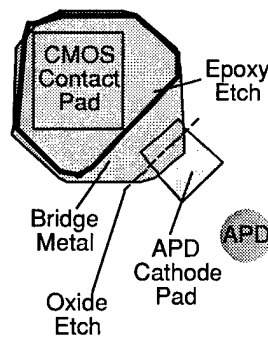
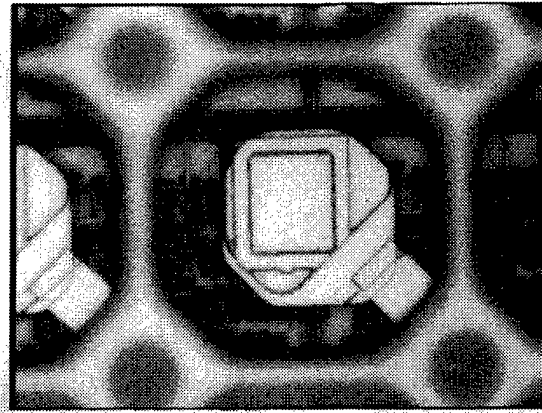
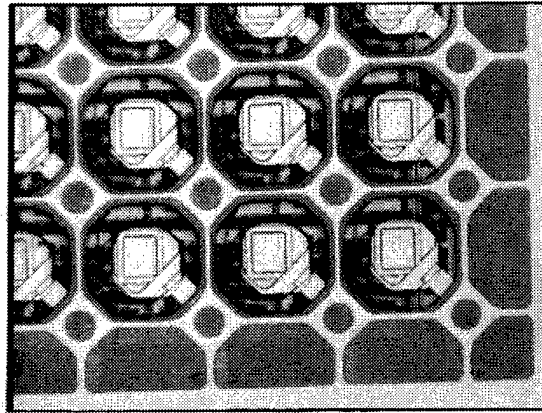


Figure 5-4. Bridge-bonded pixels viewed from the avalanche photodiode side.

6. ANALOG DEVICE TECHNOLOGY

6.1 DIGITAL LOGIC OPERATING AT DATA RATES UP TO 160 GHz

Superconducting electronic circuits based on Josephson junctions have been proposed for digital, analog, and mixed-signal electronic systems requiring operation at speeds beyond the state of the art for semiconductor circuitry. Proposals have included petaFLOP supercomputers, analog-to-digital converters, and electronic interfaces for high-speed optical communications. Demonstrated operating speeds of at least 100 GHz would probably be required before a superconductor-based implementation of one of the systems mentioned above would be attractive. To achieve these speeds, Josephson junctions with areas less than $1 \mu\text{m}^2$ must be integrated at high densities.

In this report we present the results of superconducting microelectronic circuits fabricated at Lincoln Laboratory. The circuits consisted of roughly 10 Josephson junctions, each of which had an area of $\sim 0.5 \mu\text{m}^2$. These circuits operated at speeds up to 160 GHz. They were fabricated using optical lithography and a highly manufacturable processing technology that will be easily extensible to much larger integration scales.

The fastest superconducting electronic circuits take advantage of a few of the fundamental physical properties unique to superconductivity: (1) Type I superconductors exclude magnetic flux perfectly; (2) the phase of the Cooper-pair wavefunction of the electrons around a superconducting loop is quantized in multiples of 2π , with each increasing quantum of phase corresponding to the presence of an additional magnetic fluxon ($\Phi_0 \sim 2.07 \times 10^{-15}$ webers) in the loop; and (3) high-speed signals propagate in superconducting transmission lines on-chip essentially without dispersion or loss. Digital information in these circuits is encoded in the propagation of magnetic fluxons around the circuits—the arrival or lack of arrival of a fluxon at a circuit node during a given clock pulse corresponds to a “1” or a “0” at that circuit node. Circuits that operate using fluxons to transport their digital information are referred to as rapid single-flux quantum (RSFQ) circuits. In recent years several impressive high-speed circuit demonstrations have been performed using RSFQ, including evidence of operation up to 750 GHz [1]. All of these high-speed demonstrations have relied upon electron-beam lithography for device patterning, and have focused on demonstration of small-scale circuits.

Figure 6-1 shows a schematic cross section of the Lincoln Laboratory low-temperature (4.2 K) superconducting electronics process used to fabricate the circuits. This process was adapted from the doubly planarized all-refractory superconducting technology (DPARTS) [2]. Optical i-line lithography is employed at every pattern-definition step, and chemical-mechanical planarization is used to form self-aligned contacts to the junction's counter-electrode level. The pattern definition is capable of resolving features in photoresist down to $0.4 \mu\text{m}$, but our process used slightly more conservative design rules, with $1.0\text{-}\mu\text{m}$ linewidths on a $1.7\text{-}\mu\text{m}$ pitch and $0.8\text{-}\mu\text{m}^2$ Josephson junctions. The junctions were formed in a Nb/AlO_x/Nb trilayer, the wiring and inductors were made of niobium, and the resistors were fashioned from a Pt/Ti film. The junctions had a critical current density J_c of 20 kA/cm^2 and the resistors had a nominal sheet resistance of $0.6 \Omega/\text{square}$.

Shown in Figure 6-2 is an optical micrograph of the circuit that we used to demonstrate the high operating speeds that we observed: a simple T flip-flop. This circuit took a dc input current, converted it into a stream of bits whose frequency was roughly proportional to the input current, and then toggled the input bit stream between two independent output bit streams. The result was two output channels, each with one half the bit frequency of the input channel. The average voltage of the input bit stream and one of the output bit streams was then measured. Because magnetic fluxons were used to carry bits through the circuit, the time-averaged voltage at the input or output inductor was directly proportional to the bit rate of the data, with a constant of proportionality fixed by the fundamental Josephson relation at 483 GHz/mV. (The voltage standard is defined using the inverse of this effect: a known frequency is applied and the resulting voltage is determined precisely. In our case a voltage was measured from which the frequency of oscillation was determined precisely.)

In Figure 6-3 the measured voltages at the input and output of the T flip-flop are plotted as a function of input current. The difference between the input voltage and twice the output voltage is shown on the right-hand axis. Because the input bit stream was exactly double the output bit stream, the output voltage was exactly half the input voltage at voltages up to $\sim 330 \mu\text{V}$ (corresponding to bit rates of 160 GHz), at which point the circuit ceased to function properly. We obtained the data by holding the input current at a fixed level, and then digitally averaging multiple measurements of the input and output voltages before moving to the next input current level. We then subtracted a fixed offset from the data to compensate for offsets inherent to the measurement apparatus.

The operating speeds and integration scales achieved here are by no means the limit of this technology. We expect that improved circuit optimization, including steps to reduce inductive parasitic effects and especially to further decrease the junction size and therefore the junction capacitance, would substantially increase the operating speed. We also expect that the existing process could accommodate larger integration scales without improvements, and that further process optimization centered on improved linewidth control in lithography and etch might allow integration scales into the thousands or even millions of junctions.

K. K. Berggren	M. J. O'Hara
D. A. Feld	E. M. Macedo
T. J. Weir	

REFERENCE

1. W. Chen, A. V. Rylyakov, V. Patel, J. E. Lukens, and K. K. Likharev, *Appl. Phys. Lett.* **73**, 2817 (1998).
2. K. K. Berggren, E. M. Macedo, D. A. Feld, and J. P. Sage, *IEEE Trans. Appl. Supercond.* **9**, 3271 (1999).

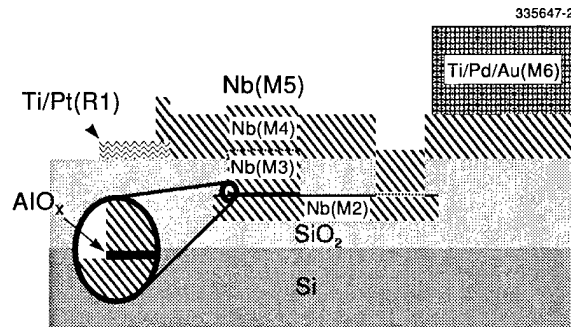


Figure 6-1. Schematic cross section of the existing Lincoln Laboratory superconducting electronics process showing the Nb(M2)/AlO_x/Nb(M3) trilayer, the Pt/Ti (R1) resistors, the Nb wiring (M4) layer, and the self-aligned contact to the counter-electrode (M3) layer.

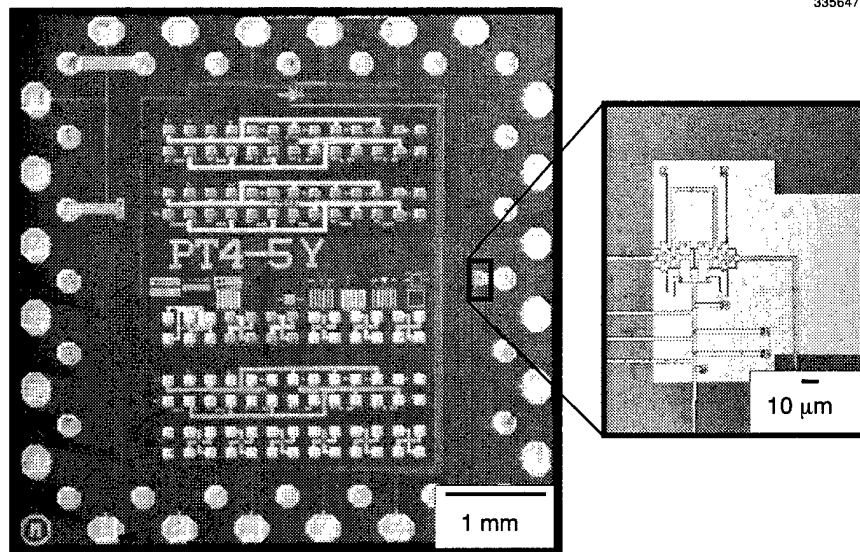


Figure 6-2. Optical micrograph showing a superconducting chip as fabricated at Lincoln Laboratory. The chip fits in a 24-pin probe that is immersed in liquid helium for testing at 4.2 K. The expanded region is a photomicrograph showing the detailed layout of the tested circuit.

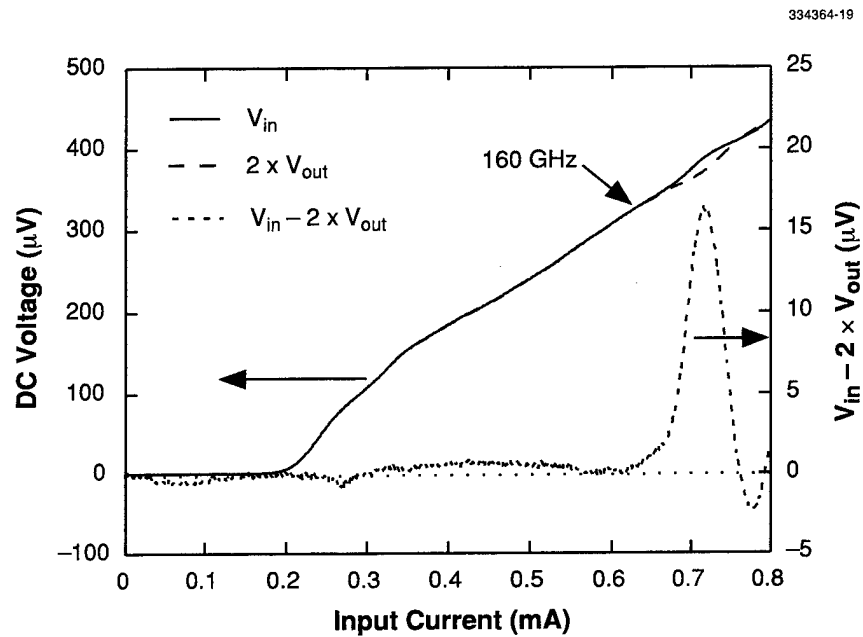


Figure 6-3. Along the left axis, the input voltage V_{in} and twice the output voltage V_{out} were plotted against the input current to show that the frequency of the output bit stream was exactly half the frequency of the input bit stream. Along the right axis, the difference between twice V_{out} and V_{in} is plotted on a 10 \times magnified scale to show the clear departure from zero, corresponding to failure of proper circuit operation, above 330 μV or 160 GHz.

7. ADVANCED SILICON TECHNOLOGY

7.1 NEW LOW-POWER 0.35- μm CCD/FDSOI-CMOS TECHNOLOGY

The first known demonstration of charge-coupled device (CCD) imager and fully depleted silicon-on-insulator (FDSOI) CMOS fabrication on the same 150-mm-diam wafer is reported. This new 3.3-V, 0.35- μm low-power technology is a descendent of Lincoln Laboratory's 10-V, high-sensitivity CCD [1] and 2-V, 0.25- μm FDSOI-CMOS [2] processes. Its function is to fabricate low-power, compact imaging systems. Modifications were made in device design to accommodate the shared voltage requirements of the new process. The 3.3-V operation required modifications to CCD and FDSOI device designs in order to maintain the 10-V CCD charge-transfer and collection efficiency and to increase the operating voltage of the 2-V FDSOI technology. In addition, further process modifications were necessary to satisfy the united fabrication requirements of critical dimension control, etch profile and selectivity, slip control, and back-end planarization.

A schematic cross section of the merged CCD/FDSOI-CMOS structure is presented in Figure 7-1. Fabrication was done on 150-mm-diam Unibond SOI wafers with 190-nm buried oxide (BOX). SOI and BOX regions were selectively removed from the wafer to permit CCD fabrication in the bulk substrate wafer and FDSOI-CMOS fabrication in the thin SOI region. For deep substrate depletion and thus broad CCD spectral response, a 300- $\Omega\text{ cm}$, 30- μm -thick epitaxial layer on a p -type substrate was used as the SOI handle wafer.

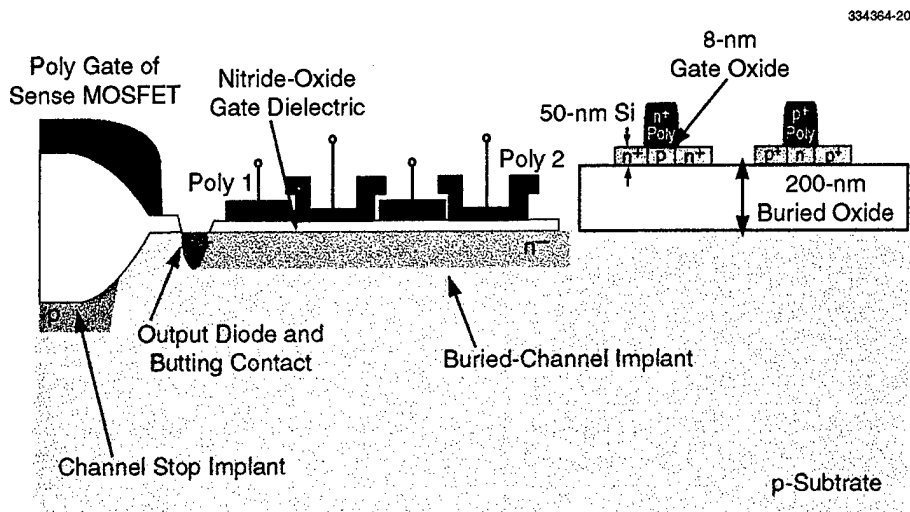


Figure 7-1. Schematic cross section of merged charge-coupled device (CCD) and 0.35- μm FDSOI-CMOS n - and p -channel transistors.



Figure 7-2. Image of Lexington Minuteman statue taken by 512×1024 , $15 \times 15\text{-}\mu\text{m}$ pixel CCD array fabricated in the new CCD/FDSOI-CMOS technology. CCD parallel and serial register clocking was done with 3.3 V.

The SOI layer was reduced from 180 nm to its final 50-nm thickness by oxidation. Isolation for bulk devices was by LOCOS and for SOI devices by mesa definition. All layers were defined with 248-nm optical lithography and plasma etch techniques. This technology includes two poly layers, three metal layers, damascene contacts and vias, and full back-end planarization. CMOS features include a 7.2-nm gate oxide; complementarily doped poly; source and drain extensions; low-pressure chemical vapor deposited TEOS oxide spacers; activation of implants by rapid thermal processing; and cobalt-silicided source, drain, and gate.

Shown in Figure 7-2 is the image obtained by projecting a slide of the historic Lexington Minuteman statue onto a front-illuminated 512×1024 -pixel, frame-transfer CCD fabricated in the merged CCD/FDSOI-CMOS process. This imager contains over 500 000 pixels. The parallel and serial register clocking was done with 3.3-V swings. Charge-transfer efficiencies at 3.3 V have been measured to be greater than 99.998% for $15 \times 15\text{-}\mu\text{m}$ pixels after 512 transfers.

Figure 7-3 compares the dark current for the CCD/FDSOI-CMOS fabricated imagers (circles) with that from imagers fabricated in Lincoln Laboratory's standard CCD process. The exponential dependence of dark current with temperature is characteristic of thermal generation in the bulk epi substrate wafer and at the epi surface. The dark current is comparable for the two processes and thus demonstrates that the additional processing required to bond SOI to the epi substrate and to fabricate high-performance FDSOI-CMOS did not create additional bulk or interface defect states. In addition, we have seen no evidence of slip in these imagers.

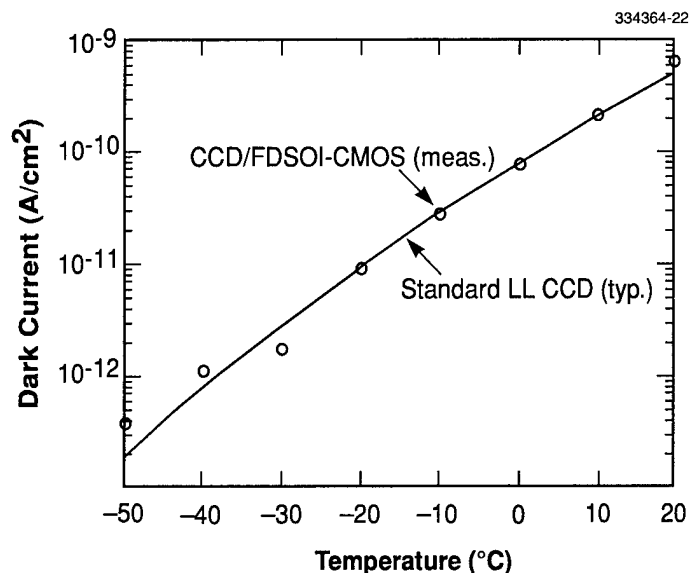


Figure 7-3. CCD dark current as a function of temperature for the new CCD/FDSOI-CMOS imagers (circles) and for the standard Lincoln Laboratory CCD-only process (line).

Typical SOI transistor output and subthreshold characteristics for devices with $W/L = 8/0.35 \mu\text{m}$ are shown in Figures 7-4(a) and 7-4(b). Note particularly that the n -MOS devices can withstand at least 4-V drain bias with no indication of punchthrough.

Figure 7-5 shows the stage delay for a typical 97 stage (fanout = 1) $0.35\text{-}\mu\text{m}$ gate length ring oscillator as a function of power supply voltage for the Lincoln Laboratory CCD/FDSOI-CMOS process (triangles) and a data point for a commercial $0.35\text{-}\mu\text{m}$ gate length, 3.3-V bulk CMOS process. For 3.3-V operation, the CCD/FDSOI-CMOS process demonstrates twice the speed of the bulk process—47 ps/stage vs 93 ps/stage. Further, for the same 93-ps stage delay, the CCD/FDSOI-CMOS process performs at 1.5 V—a 4.8 \times reduction in power relative to the bulk process.

V. Suntharalingam J. A. Burns
B. E. Burke M. J. Cooper
C. L. Keast

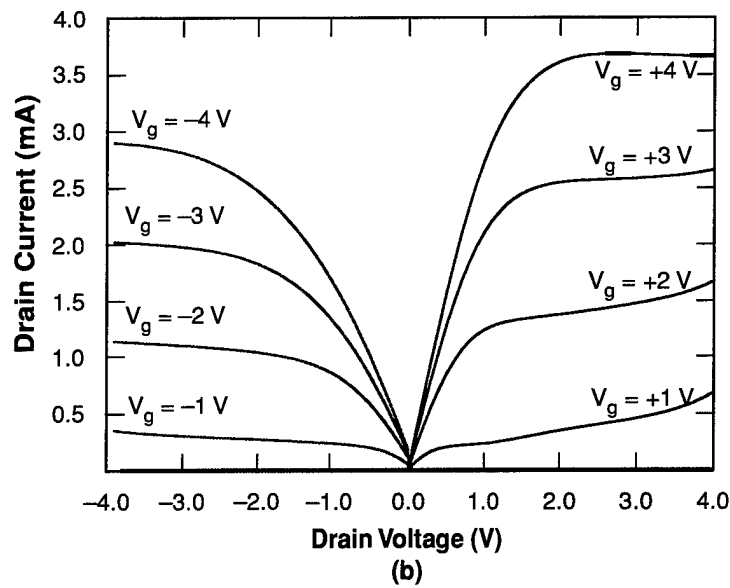
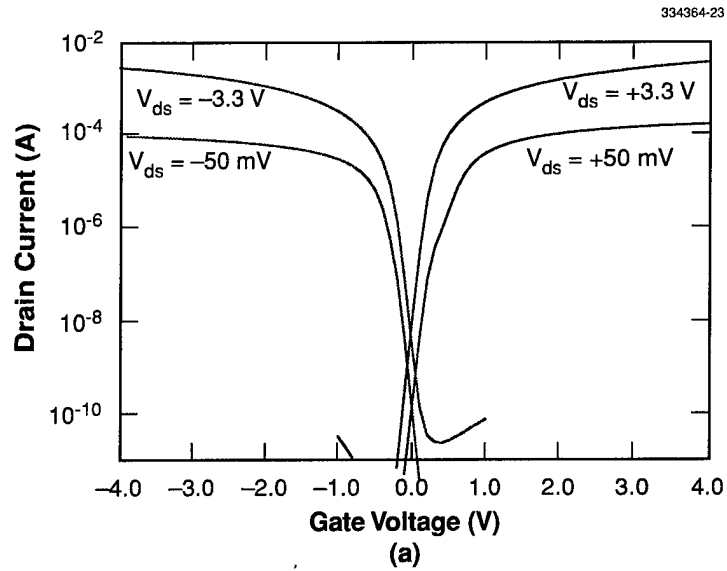


Figure 7-4. (a) Typical subthreshold characteristics for SOI CMOS devices from the CCD/FDSOI-CMOS process; $W/L = 8 \mu\text{m}/0.35 \mu\text{m}$. (b) Typical output characteristics for SOI CMOS devices from the CCD/FDSOI-CMOS process; $W/L = 8 \mu\text{m}/0.35 \mu\text{m}$.

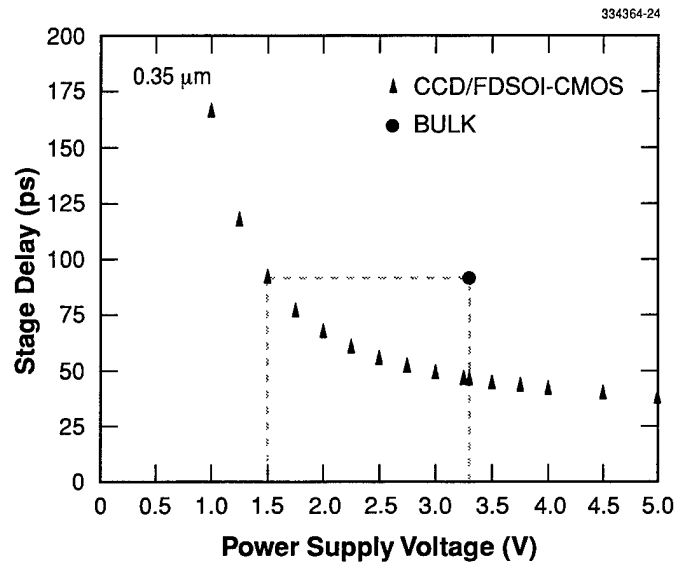


Figure 7-5. Ring oscillator (fanout = 1) stage delay as a function of power supply voltage for 0.35- μm CCD/FDSOI-CMOS (triangles) and commercial bulk CMOS (circle). For 3.3-V operation, the CCD/FDSOI-CMOS process is 2 times faster than the bulk process. For the same stage delay, the CCD/FDSOI-CMOS oscillator consumes 4.8 times less power than the commercial bulk process.

REFERENCES

1. B. E. Burke, J. A. Gregory, M. W. Bautz, G. Y. Prigozhin, S. E. Kissel, B. B. Kosicki, A. H. Loomis, and D. J. Young, *IEEE Trans. Electron Devices* **44**, 1633 (1997).
2. J. A. Burns, C. L. Keast, J. M. Knecht, R. R. Kunz, S. C. Palmateer, S. Cann, A. Soares, and D. C. Shaver, *Proceedings of IEEE International SOI Conference* (IEEE, Piscataway, N.J., 1996), p. 102.

